Lawrence Berkeley National Laboratory
Recent Work

Authors
Vogman, GV
Shumlak, U
Colella, P
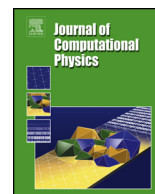
Conservative fourth-order finite-volume Vlasov–Poisson solver for axisymmetric plasmas in cylindrical (r, v_r, v_θ) phase space coordinates

G.V. Vogman [a],[*], U. Shumlak [b], P. Colella [c]

[a] *Center for High Energy Density Science, Lawrence Livermore National Laboratory, Livermore, CA, 94550, United States of America*
[b] *Aerospace & Energetics Research Program, University of Washington, Seattle, WA 98195, United States of America*
[c] *Computational Research Division, Lawrence Berkeley National Laboratory, Berkeley, CA 94720, United States of America*

A B S T R A C T

A fourth-order finite-volume Vlasov–Poisson algorithm is developed for simulating axisymmetric plasma configurations in (r, v_r, v_θ) phase space coordinates. The Vlasov equation for cylindrical phase space coordinates is cast into conservation-law form and is discretized on a structured grid. The conservative finite-volume discretization is based on fifth-order upwind reconstructions of the distribution function and a fourth-order quadrature rule that accounts for transverse variations of fluxes along control volume surfaces. High-order specular reflection boundary conditions enable high-fidelity treatment of plasma distribution functions at the axis and at wall boundaries. The numerical method is applied to simulate a confined uniform neutral gas to assess convergence properties for an equilibrium system in which effects of finite-temperature and acceleration due to centrifugal and Coriolis forces are present. The discretization is also applied to a Z-pinch configuration to study electrostatic ion confinement and the dynamics of the associated breathing mode. Simulations show that the ion distribution function exhibits non-Maxwellian features and that a temperature anisotropy develops and is sustained. The finite-volume implementation is demonstrated to converge at fourth-order for both applications.

© 2018 Elsevier Inc. All rights reserved.

1. Introduction

Kinetic theory offers one of the most complete theoretical descriptions of a plasma and treats each particle species as a probability distribution function in a six-dimensional position-velocity phase space. The evolution of each distribution function is described by the Boltzmann equation coupled to Maxwell's equations. When the dynamics of plasma particles are dominated by long-range interactions, collisions can be neglected, and the Boltzmann equation reduces to the Vlasov equation.

Numerical methods for solving the kinetic theory governing equations generally fall into one of two categories: particle-in-cell (PIC) methods and continuum methods. PIC methods are widely used and sample a species distribution function with superparticles, each of which – through its charge and mass – typically represents many physical-world particles. See Refs. [1–4], for a review of PIC methods, their development, and applications. By contrast, continuum methods define a distribution function in terms of piecewise smooth functions (e.g. polynomials) on a grid in phase space, and evolve

---

* Corresponding author.
 E-mail address: vogman1@llnl.gov (G.V. Vogman).

it by solving the Vlasov equation directly. Examples of different continuum kinetic approaches include spectral [5–7], semi-Lagrangian [8–10], finite-difference [11], finite-volume [12,13], and finite-element [14–16] discretizations. Since computational cost scales exponentially with the number of dimensions, continuum methods are computationally expensive. However, recent advances in supercomputing capability have made computational cost less of an impediment, which has resulted in significant progress in continuum kinetic discretizations, including: conservative spatial discretization [12,17,10], adaptive mesh refinement algorithms [18], mapped geometry techniques [19–21], five-dimensional simulations [22–24], and high-order spatial discretizations [25,26,12]. Continuum methods offer a number of advantages. They can be applied to the conservation-law form of the governing equations so as to guarantee local and global conservation of the distribution function. Continuum methods can also readily take advantage of high-order discretization techniques, and thereby achieve enhanced solution accuracy [13]. Unlike PIC methods, the continuum approach is not subject to noise, and can thus retain accuracy over longer periods of simulated time.

While many magnetized plasmas (e.g. field-reversed configurations, Z-pinches, Hall thrusters, spheromaks, particle beams) are axisymmetric, kinetic simulations are often performed in Cartesian phase space coordinates, which are simpler to treat numerically, but cannot take advantage of axisymmetry. A continuum kinetic simulation of an axisymmetric plasma in Cartesian coordinates would require modeling a six-dimensional phase space, which presently amounts to a prohibitive computational expense. In certain limiting cases, the problem of computational cost can be mitigated. For example, in the limit of a strong magnetic field gyrokinetic approximations can be applied to average over particle Larmor orbits so as to reduce a 6D phases space representation to three position and two velocity dimensions (one parallel and one perpendicular to the magnetic field). Such approximations have been successfully applied to model low-frequency dynamics in tokamaks [23,24]. In configurations without a strong guide field, gyrokinetic assumptions do not apply, and computational cost cannot be reduced through gyroaveraging. For example, in an axisymmetric Z-pinch the magnetic field can vary from zero at the axis to a peak value off-axis, such that Larmor orbits vary considerably and the three velocity dimensions cannot be reduced to two.

A number of approaches have been developed to model plasmas in cylindrical geometries while retaining the full kinetic treatment of at least one species. Techniques have been developed for PIC methods to handle particles traversing cells with non-uniform volumes, including: specialized weighting and interpolation [27–30], procedures involving recurring mapping from Cartesian to cylindrical or to curvilinear geometry [31–33], advancing particles in three dimensions for axisymmetric configurations to circumvent problems at the axis [34], and combinations of these techniques [35]. Applications of various PIC methods to axisymmetric and cylindrically symmetric configurations include high-power microwaves [36–40], Hall thrusters [41–43], wakefield accelerators [44,35], particle beams [45–47], pulsed-power configurations [48–51], Z-pinches [52–56], and field-reversed configurations [57,58]. Research literature on continuum kinetic methods for discretizing cylindrical phase space coordinates is extremely sparse and typically does not include convergence studies, making it difficult to assess generalizability. Examples include semi-Lagrangian methods for modeling axisymmetric charge-dominated beam plasmas [59] and finite-difference methods for modeling plasma edge dynamics [61], high frequency electrostatic waves in a uniform magnetic field [62], and rarefied gas dynamics [63,64,60].

To address the need for robust numerical methods that exploit axisymmetry, this paper presents a high-order accurate continuum kinetic approach for discretizing the cylindrical coordinate Vlasov equation in a way that ensures conservation of the distribution function. A conservation-law form of the cylindrical coordinate Vlasov equation is derived, and a fourth-order conservative finite-volume discretization is developed and applied to simulate axisymmetric electrostatic systems. Nuances associated with boundary conditions, centrifugal and Coriolis forces, and finite-volume quadrature rules are described in detail. The numerical formulation is applied to model a neutral gas and electrostatic ion confinement in a Z-pinch configuration. The techniques described for (r, v_r, v_θ) phase space coordinates can be easily extended to 2D3V $(r, z, v_r, v_\theta, v_z)$ simulations, and thereby lay important foundations for capturing the dynamics of more generalized axisymmetric plasmas.

This paper is organized as follows. Section 2 presents the derivation of the conservation-law form of the Vlasov equation in full six-dimensional cylindrical phase space coordinates. Axis and wall boundary conditions for axisymmetric configurations are described. The fourth-order finite-volume discretization of the cylindrical coordinate Vlasov equation is presented in Sec. 3 and includes a discussion of quadrature rule evaluation, boundary condition implementation, time step constraints, and Poisson solver for the electrostatic potential. Applications of the algorithm are presented in Sec. 4. The cylindrical coordinate solver is applied to simulate a spatially uniform neutral gas to assess convergence properties and numerical errors. The algorithm is also applied to model electrostatic ion confinement in a one-dimensional Z-pinch configuration and is shown to agree with physically expected behavior. The detailed evolution of the ion distribution function, development of temperature anisotropy, and development of multimodal structures caused by phase mixing are described. Fourth-order accuracy is demonstrated for both applications.

2. Governing equations in conservation-law form

In kinetic theory of plasmas, each particle species s is represented by a probability distribution function $f_s(\boldsymbol{x}, \boldsymbol{v}, t)$ in a position velocity phase space. If the plasma is collisionless, then the evolution of the distribution function is described by the Vlasov equation, coupled to Maxwell's equations. It is advantageous to express the Vlasov equation in conservation-law form, which can be numerically solved in a way that exactly satisfies the discrete form of the divergence theorem. This

ensures that the distribution function and its zeroth velocity moment, from which charge density is computed, are conserved to machine precision. The resulting conservation of charge is critical for accurate modeling of dynamics in plasmas since the motion of charged species couples to the evolution of electromagnetic fields. The conservation-law form of the Vlasov equation for Cartesian coordinates $\mathbf{X} = \left[x, y, z, v_x, v_y, v_z\right]^T$ is

$$0 = \frac{\partial f_s}{\partial t} + \nabla_{\mathbf{X}} \cdot \left(\dot{\mathbf{X}} f\right), \tag{1}$$

where $\dot{\mathbf{X}} = \left[v_x, v_y, v_z, a_x, a_y, a_z\right]^T$ with $\{a_x, a_y, a_z\}$ being the components of the acceleration due to the Lorentz force. The conservation-law form of the Vlasov equation in cylindrical phase space coordinates can be derived using the mapping from Cartesian to cylindrical $\boldsymbol{\xi} = [r, \theta, z, v_r, v_\theta, v_z]^T$ coordinates:

$$\boldsymbol{\xi} = \boldsymbol{\xi}\left(\mathbf{X}\right) = \left[(x^2 + y^2)^{1/2}, \arctan\left(\tfrac{y}{x}\right), z, \tfrac{v_x x + v_y y}{(x^2 + y^2)^{1/2}}, \tfrac{v_y x - v_x y}{(x^2 + y^2)^{1/2}}, v_z\right]^T. \tag{2}$$

Let $\bar{\mathbf{F}} = \dot{\mathbf{X}} f_s$ denote the six-element flux vector in Cartesian coordinates. The divergence of a vector field in Cartesian coordinates can be rewritten in terms of derivatives in a different coordinate system provided that there is a smooth mapping between the two coordinate systems [65,66]. The divergence of fluxes in Eq. (1) can thereby be expressed in terms of cylindrical coordinates using the relation

$$\nabla_{\mathbf{X}} \cdot \bar{\mathbf{F}} = J \nabla_{\boldsymbol{\xi}} \cdot \left(\frac{1}{J}\left(\frac{\partial \boldsymbol{\xi}}{\partial \mathbf{X}}\right)\bar{\mathbf{F}}\right) \tag{3}$$

$$J = \det\left(\frac{\partial \boldsymbol{\xi}}{\partial \mathbf{X}}\right) = \frac{1}{r} \tag{4}$$

where $\frac{\partial \boldsymbol{\xi}}{\partial \mathbf{X}}$ is the Jacobian matrix of transformation. The conservation-law form of the Vlasov equation in cylindrical coordinates is then

$$0 = \frac{\partial f_s}{\partial t} + \frac{1}{r}\frac{\partial}{\partial r}\left(r v_r f_s\right) + \frac{1}{r}\frac{\partial}{\partial \theta}\left(v_\theta f_s\right) + \frac{\partial}{\partial z}\left(v_z f_s\right)$$
$$+ \frac{\partial}{\partial v_r}\left(\left[a_r + \frac{v_\theta^2}{r}\right] f_s\right) + \frac{\partial}{\partial v_\theta}\left(\left[a_\theta - \frac{v_r v_\theta}{r}\right] f_s\right) + \frac{\partial}{\partial v_z}\left(a_z f_s\right), \tag{5}$$

where v_θ^2/r is the acceleration due to the centrifugal force, $-v_r v_\theta/r$ is the acceleration due to the Coriolis force, and $\{a_r, a_\theta, a_z\}$ are the components of acceleration due to the Lorentz force along each coordinate direction. Thus the flux vector in cylindrical coordinates is

$$\mathbf{F} = \dot{\boldsymbol{\xi}} f_s = \left[v_r f_s, v_\theta f_s, v_z f_s, \left(a_r + \frac{v_\theta^2}{r}\right) f_s, \left(a_\theta - \frac{v_r v_\theta}{r}\right) f_s, a_z f_s\right]^T. \tag{6}$$

Carrying out the differentiation for each term in Eq. (5) yields

$$0 = \frac{\partial f_s}{\partial t} + v_r\frac{\partial f_s}{\partial r} + \frac{v_\theta}{r}\frac{\partial f_s}{\partial \theta} + v_z\frac{\partial f_s}{\partial z} + \left[a_r + \frac{v_\theta^2}{r}\right]\frac{\partial f_s}{\partial v_r} + \left[a_\theta - \frac{v_\theta v_r}{r}\right]\frac{\partial f_s}{\partial v_\theta} + a_z\frac{\partial f_s}{\partial v_z}, \tag{7}$$

which is the standard non-conservative form of the cylindrical coordinate Vlasov equation [67,68,60,59,69]. Equation (7) can be derived using Christoffel symbols [67], Lamé coefficients [68], or the mapping in Eq. (2). It is worth noting that the cylindrical coordinate Vlasov equation is rarely expressed in conservation-law form (see for example Ref. [70]) likely because the standard form is easier to analyze and because conservative numerical discretizations of the Vlasov equation have largely been tailored toward Cartesian coordinates. A modified conservative form, in which velocity coordinates v_r and v_θ are mapped to a polar grid, is presented in Refs. [63,64,60] in application to rarefied gas dynamics.

For an electrostatic plasma the Lorentz acceleration is due to the electric field $\mathbf{E} = -\nabla\phi$. The electrostatic potential ϕ is computed from the Poisson equation, which in non-dimensionalized form [13,71] is

$$-\nabla \cdot (\nabla\phi) = \sum_s Z_s n_s \tag{8}$$

$$n_s = \int_{-\infty}^{\infty}\int_{-\infty}^{\infty}\int_{-\infty}^{\infty} f_s \, dv_r dv_\theta dv_z, \tag{9}$$

where $Z_s = q_s/|e|$ is the ionization state (i.e. the ratio of the charge of species s to the electron charge) and n_s is the number density of species s computed from the zeroth velocity moment of the distribution function. For this choice of

non-dimensionalization, time is normalized to the ion plasma frequency ω_{pi}, lengths are normalized to the experimental spatial scale L, velocities are normalized to the product $L\omega_{pi}$, and the potential is normalized to the characteristic value $\phi_0 = e n_0 L^2 / \epsilon_0$, where n_0 is the characteristic number density and ϵ_0 is the permittivity of free space.

The axisymmetric plasma of interest is assumed to be uniform in the z direction, such that it can be modeled in (r, v_r, v_θ) phase space coordinates. Thus for the computational studies conducted here, the governing equation is the non-dimensionalized Vlasov equation in three phase space coordinates:

$$0 = \frac{\partial f_s}{\partial t} + \frac{1}{r} \frac{\partial}{\partial r} (r v_r f_s) + \frac{\partial}{\partial v_r} \left(\left[\frac{Z_s}{M_s} E_r + \frac{v_\theta^2}{r} \right] f_s \right) + \frac{\partial}{\partial v_\theta} \left(\left[-\frac{v_r v_\theta}{r} \right] f_s \right), \tag{10}$$

where E_r is computed from the potential given by Eq. (8) and M_s is the ratio of the mass of species s to the ion mass. Henceforth the subscript s is omitted for clarity.

2.1. Boundary conditions for the distribution function

Solutions to the Vlasov–Poisson equation system are subject to initial conditions and boundary conditions. For the numerical investigations conducted here, the scope of physical boundary conditions [72–75] is limited to an axis boundary at $r = 0$ and a reflecting wall boundary at the outer radius. The latter is, in effect, the free-slip wall boundary condition often used in fluid simulations.

Since collisions are not modeled by the Vlasov–Poisson equation system, a pure specular reflection boundary condition can be applied in the case of both a wall [73] and an axis of symmetry [74]. For a point $\boldsymbol{x}$ on a boundary $\partial\Omega$ of an arbitrary region Ω, the specular reflection condition on the distribution function is

$$f(\boldsymbol{x}, \boldsymbol{v}, t) = f(\boldsymbol{x}, \boldsymbol{v} - 2(\boldsymbol{v} \cdot \hat{\boldsymbol{n}})\hat{\boldsymbol{n}}, t), \qquad \hat{\boldsymbol{n}} \cdot \boldsymbol{v} < 0, \qquad \boldsymbol{x} \in \partial\Omega, \tag{11}$$

where $\hat{\boldsymbol{n}}$ is the outward normal vector of $\partial\Omega$ (pointing out of Ω) at point $\boldsymbol{x}$. Physically this means that any plasma particles that impinge upon the axis or wall boundary are reflected, with the original normal component of velocity changing sign. In effect the normal drift velocity of particles at the axis or at a wall must be zero and information from the appropriate velocity half-plane must be used when setting a boundary condition on f.

In addition to physical-space boundary conditions, it is important to consider velocity-space boundaries. While analytically the velocity domain is infinite, for the purposes of numerical simulations the velocity domain is truncated at a finite velocity $v_{\max}$, such that $\boldsymbol{v} \in [-v_{\max}, v_{\max}] \times [-v_{\max}, v_{\max}] \times [-v_{\max}, v_{\max}]$. This truncation can be physically justified if the dynamics of plasma particles fall well within a finite velocity range. The choice of the value of $v_{\max}$ is important because velocity boundaries should be far enough away so as not to affect the evolution of f. Numerically this can be guaranteed if $f(\pm v_{\max})$ is zero to machine precision for all simulated time. If $f(\pm v_{\max})$ is non-zero, then in flux-based simulations the distribution function can "leak" through the velocity boundaries. At the same time, $v_{\max}$ can dictate the magnitude of the maximum advection speed in the system, which for numerical simulations places a constraint on the time step size. Consequently $v_{\max}$ should be small enough to ensure that simulations are feasible. In practice, $v_{\max}$ is determined empirically to satisfy these constraints. To prevent any loss/gain of the distribution function through the velocity boundaries, i.e. to ensure conservation of the distribution function on a finite velocity domain, the flux at velocity boundaries is set to zero.

3. Fourth-order finite-volume discretization

The discretization of the cylindrical coordinate Vlasov–Poisson system is carried out using a fourth-order accurate finite-volume method on a structured grid combined with a fourth-order explicit Runge–Kutta method for time advance. The spatial discretization is based on the method described in Refs. [65,76], aspects of which have been applied to the Vlasov equation in Cartesian coordinates [12,18,13] and to gyrokinetics in annular domains [77,20,21]. Here the method is modified to explicitly account for volume variation with radius without mapping to a Cartesian grid. This enables robust treatment of the axis boundary. The method is distinct from high-order finite-volume discretizations based on Gaussian quadrature [78], essentially non-oscillatory [78], central essentially non-oscillatory [79], weighted essentially non-oscillatory [80,81], and arbitrary derivative Riemann problem (ADER) [82,83] methods.

Let each control volume be defined by its cell-center multi-index $\boldsymbol{i} = (i_1, i_2, i_3, \cdots, i_D)$, where D is the number of phase space dimensions being modeled. The center of a cell face is designated by multi-index $\boldsymbol{i} + \frac{1}{2}\boldsymbol{e}^d$, where $\boldsymbol{e}^d$ denotes the unit vector in the d-th direction. Let $\langle \cdot \rangle_{\boldsymbol{i}}$ denote the volume integral, and let $\langle \cdot \rangle_{\boldsymbol{i}+\frac{1}{2}\boldsymbol{e}^d}$ denote the surface integral over a face centered at $\boldsymbol{i} + \frac{1}{2}\boldsymbol{e}^d$ whose normal points in the d-th direction. Integrating the Vlasov equation over a cell and applying the divergence theorem yields the discrete flux-based form of the Vlasov equation

$$\frac{\partial}{\partial t} \langle f \rangle_{\boldsymbol{i}} = -\sum_{d=1}^{D} \left(\left\langle F^d \right\rangle_{\boldsymbol{i}+\frac{1}{2}\boldsymbol{e}^d} - \left\langle F^d \right\rangle_{\boldsymbol{i}-\frac{1}{2}\boldsymbol{e}^d} \right), \tag{12}$$

where the cell-integrated distribution function is the primary variable and is defined as
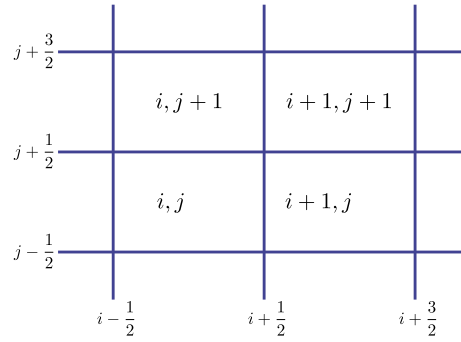
Fig. 1. Index notation for a regular grid in two dimensions with generic cell (i, j), its faces at $i \pm \frac{1}{2}$ and $j \pm \frac{1}{2}$, and its neighboring cells.

$$\langle f \rangle_{\boldsymbol{i}} = \int_{V_{\boldsymbol{i}}} f r \, dr \, d\theta \, dz \, dv_r \, dv_\theta \, dv_z, \tag{13}$$

F^d is the flux along the d-th coordinate direction (see Eq. (6)), and the face-integrated flux is defined as

$$\left\langle F^d \right\rangle_{\boldsymbol{i}+\frac{1}{2}\boldsymbol{e}^d} = \int_{S_{\boldsymbol{i}+\frac{1}{2}\boldsymbol{e}^d}} F^d \, dS, \tag{14}$$

where $S_{\boldsymbol{i}+\frac{1}{2}\boldsymbol{e}^d}$ is the surface of the $\boldsymbol{i}+\frac{1}{2}\boldsymbol{e}^d$ cell face. Note that in phase space a surface can have more than two dimensions and surface areas with normals in the radial direction change with radius. Unlike Refs. [65,76,13], which use cell-average and face-average quantities, cell-integrated and face-integrated quantities are used here for ease of handling directionally-dependent stencils and quadratures.

Face integrals of fluxes, as defined in Eq. (14), are computed through a two-step process. The first step is a one-dimensional fifth-order upwind polynomial interpolation of $\langle f \rangle_{\boldsymbol{i}}$ to cell faces to obtain $\langle f \rangle_{\boldsymbol{i}+\frac{1}{2}\boldsymbol{e}^d}$. The second step is the application of a fourth-order accurate quadrature rule for computing integrals of products over cell faces, which relies on computing point values from face-integrated values. Using Taylor series, the face integral $\langle f \rangle_{\boldsymbol{i}+\frac{1}{2}\boldsymbol{e}^d}$ is related to the point value $f_{\boldsymbol{i}+\frac{1}{2}\boldsymbol{e}^d}$ at the center of the face through the expression

$$\langle f \rangle_{\boldsymbol{i}+\frac{1}{2}\boldsymbol{e}^d} = \left[\tilde{r} f_{\boldsymbol{i}+\frac{1}{2}\boldsymbol{e}^d} + \sum_{d' \neq d} \left(\frac{h_{d'}^2}{24} \frac{\partial^2 (\tilde{r} f)}{\partial \xi_{d'}^2} \bigg|_{\xi_{\boldsymbol{i}+\frac{1}{2}\boldsymbol{e}^d}} + \mathcal{O}(h_{d'}^4) \right) \right] \prod_{d' \neq d} h_{d'}, \tag{15}$$

where $h_{d'}$ denotes the cell width along the d'-th coordinate direction, and $\tilde{r}$ is the Jacobian, which in this case is the radius at the center of the $\boldsymbol{i}+\frac{1}{2}\boldsymbol{e}^d$ cell face. The derivative term need only be evaluated to second-order accuracy, which can be achieved using a central difference approximation [65]. The face integral of the flux, which is a product of f and a given advection speed α, can be computed to fourth-order using the same relation, such that

$$\langle \alpha f \rangle_{\boldsymbol{i}+\frac{1}{2}\boldsymbol{e}^d} = \left[\tilde{r} \alpha_{\boldsymbol{i}+\frac{1}{2}\boldsymbol{e}^d} f_{\boldsymbol{i}+\frac{1}{2}\boldsymbol{e}^d} + \sum_{d' \neq d} \left(\frac{h_{d'}^2}{24} \frac{\partial^2 (\tilde{r} \alpha f)}{\partial \xi_{d'}^2} \bigg|_{\xi_{\boldsymbol{i}+\frac{1}{2}\boldsymbol{e}^d}} + \mathcal{O}(h_{d'}^4) \right) \right] \prod_{d' \neq d} h_{d'}. \tag{16}$$

Thus after interpolation, Eq. (15) and Eq. (16) are used in combination to compute flux integrals over faces. The details of the flux calculation are presented below for the radial direction and one non-radial direction (indexed by i and j, respectively). See Fig. 1 for an illustration of the grid indexing. The procedure extends directly to other non-radial directions, such that discretization along the z, v_r, v_θ, and v_z directions can be handled in the same way.

3.1. One-dimensional upwind polynomial interpolation

For enhanced numerical stability, the cell-integrated primary variable $\langle f \rangle_{\boldsymbol{i}}$ is interpolated to cell faces using a one-dimensional fifth-order upwind polynomial reconstruction. High-order methods require the inclusion of high-order dissipation to damp Fourier modes whose motion is poorly represented. For classical even-order methods, this is achieved by the addition of an explicit high-order dissipation to the flux. For odd-order methods, the dissipation is part of the truncation error of the operator, and is more robust [84]. Since the wave speeds in the system are simply the advection speeds along

each of the coordinate directions, the direction of advection at any given cell face is well-defined. Along the non-radial directions the same interpolation procedure is applied as in Cartesian coordinates [13], whereas interpolation along the radial direction requires weighting by the radius.

For non-radial directions, the fifth-order upwind interpolation stencil for evaluating f at face $j + \frac{1}{2}$ is given by [13,84]

$$
\langle f \rangle_{i,j+\frac{1}{2}} =
\begin{cases}
\dfrac{1}{60h_\xi}\left(2\langle f\rangle_{i,j-2} - 13\langle f\rangle_{i,j-1} + 47\langle f\rangle_{i,j} + 27\langle f\rangle_{i,j+1} - 3\langle f\rangle_{i,j+2}\right) & \text{if } \alpha_{i,j+\frac{1}{2}} > 0 \\
\dfrac{1}{60h_\xi}\left(-3\langle f\rangle_{i,j-1} + 27\langle f\rangle_{i,j} + 47\langle f\rangle_{i,j+1} - 13\langle f\rangle_{i,j+2} + 2\langle f\rangle_{i,j+3}\right) & \text{if } \alpha_{i,j+\frac{1}{2}} < 0
\end{cases}
\tag{17}
$$

where $\alpha_{i,j+\frac{1}{2}}$ is the advection speed at the $(i, j + \frac{1}{2})$ cell face. If the advection speed is zero then either stencil, or the average of the two stencils in Eq. (17) can be used.

For the radial direction, the advection speed is given by the local coordinate v_r. Let P_4 be a fourth degree polynomial, such that

$$
P_4(r) = p_4 r^4 + p_3 r^3 + p_2 r^2 + p_1 r + p_0.
\tag{18}
$$

The coefficients $\{p_4, p_3, p_2, p_1, p_0\}$ are determined by solving a linear system of five equations that relate values of the cell-integrated distribution function, which are known, to the polynomial reconstruction within the same cell. The equations are given by

$$
\langle f \rangle_{i+m,j} = \int_{r_{i+m-\frac{1}{2}}}^{r_{i+m+\frac{1}{2}}} P_4(r)\, r\, dr
\tag{19}
$$

with $m = \{-2, -1, 0, 1, 2\}$ used for $v_r > 0$ and $m = \{-1, 0, 1, 2, 3\}$ for $v_r < 0$. Solving for the coefficients of P_4 and evaluating the resulting polynomial at the $(i + \frac{1}{2}, j)$ cell face yields the stencil for $v_r > 0$:

$$
\begin{aligned}
\langle f \rangle_{i+\frac{1}{2},j} = \frac{\ell}{60 h_r(-12 + 8\ell + 45\ell^2 - 20\ell^3 - 15\ell^4 + 6\ell^5)} \Bigg[& \\
\big(16 - 40\ell^2 + 12\ell^4 \big)\langle f\rangle_{i-2,j} & \\
+ \big(-164 - 45\ell + 380\ell^2 + 75\ell^3 - 78\ell^4\big)\langle f\rangle_{i-1,j} & \\
+ \big(1276 + 1395\ell - 1300\ell^2 - 525\ell^3 + 282\ell^4\big)\langle f\rangle_{i,j} & \\
+ \big(-684 + 1395\ell - 180\ell^2 - 525\ell^3 + 162\ell^4\big)\langle f\rangle_{i+1,j} & \\
+ \big(36 - 45\ell - 60\ell^2 + 75\ell^3 - 18\ell^4\big)\langle f\rangle_{i+2,j} \Bigg], &
\end{aligned}
\tag{20}
$$

where the index ℓ is defined as

$$
\ell = \frac{r_{i+\frac{1}{2}}}{h_r}
\tag{21}
$$

and denotes the number of cell spacings away from the axis. Analogously, the stencil for $v_r < 0$ is:

$$
\begin{aligned}
\langle f \rangle_{i+\frac{1}{2},j} = \frac{\ell}{60 h_r(12 + 8\ell - 45\ell^2 - 20\ell^3 + 15\ell^4 + 6\ell^5)} \Bigg[& \\
\big(36 + 45\ell - 60\ell^2 - 75\ell^3 - 18\ell^4\big)\langle f\rangle_{i-1,j} & \\
+ \big(-684 - 1395\ell - 180\ell^2 + 525\ell^3 + 162\ell^4\big)\langle f\rangle_{i,j} & \\
+ \big(1276 - 1395\ell - 1300\ell^2 + 525\ell^3 + 282\ell^4\big)\langle f\rangle_{i+1,j} & \\
+ \big(-164 + 45\ell + 380\ell^2 - 75\ell^3 - 78\ell^4\big)\langle f\rangle_{i+2,j} & \\
+ \big(16 - 40\ell^2 + 12\ell^4\big)\langle f\rangle_{i+3,j} \Bigg]. &
\end{aligned}
\tag{22}
$$

Note that interpolation along the radial direction involves coefficients that depend on the distance from the axis, whereas the stencils for interpolation along the non-radial direction (see Eq. (17)) are coordinate independent. Note also that the coefficients in the upwind stencil given by Eq. (20) are not simply those in Eq. (22) with order reversed, but involve changes in sign as a result of the radially-weighted polynomial reconstruction in Eq. (19).

3.2. Fourth-order quadrature for face-integrated flux

The face-integrated values of the primary variable obtained from interpolation are used in combination with Eqs. (15) and (16) to compute face-integrated fluxes to fourth-order accuracy. This involves undoing face integrals of the primary variable, and computing integrals of the product of the primary variable and the advection speed.

The flux in the non-radial direction is $\langle F \rangle_{i,j+\frac{1}{2}} = \langle \alpha f \rangle_{i,j+\frac{1}{2}}$, and is evaluated by first computing the point value $f_{i,j+\frac{1}{2}}$ from the face-integrated value $\langle f \rangle_{i,j+\frac{1}{2}}$ using Eq. (15), such that

$$f_{i,j+\frac{1}{2}} = \frac{1}{r_i h_r} \left(\langle f \rangle_{i,j+\frac{1}{2}} - \frac{1}{24} \left[\langle f \rangle_{i+1,j+\frac{1}{2}} - 2 \langle f \rangle_{i,j+\frac{1}{2}} + \langle f \rangle_{i-1,j+\frac{1}{2}} \right] \right), \tag{23}$$

where the terms in the square brackets need only be evaluated to second-order accuracy. The point value of the advection speed α is readily evaluated at the center of the cell face, since α depends on local coordinates and/or the electric field, whose point value is known from the solution of Poisson's equation. The flux in the non-radial direction is then computed using the relation in Eq. (16), such that

$$\langle F \rangle_{i,j+\frac{1}{2}} = r_i \alpha_{i,j+\frac{1}{2}} f_{i,j+\frac{1}{2}} h_r + \frac{1}{24} \left[\alpha_{i+1,j+\frac{1}{2}} \langle f \rangle_{i+1,j+\frac{1}{2}} - 2 \alpha_{i,j+\frac{1}{2}} \langle f \rangle_{i,j+\frac{1}{2}} + \alpha_{i-1,j+\frac{1}{2}} \langle f \rangle_{i-1,j+\frac{1}{2}} \right]. \tag{24}$$

Analogously, the flux in the radial direction, $\langle F \rangle_{i+\frac{1}{2},j} = \langle v_r f \rangle_{i+\frac{1}{2},j}$, is evaluated by first computing $f_{i+\frac{1}{2},j}$ to fourth-order accuracy from face-integrated values using the relation in Eq. (15), such that

$$f_{i+\frac{1}{2},j} = \frac{1}{r_{i+\frac{1}{2}} h_\xi} \left(\langle f \rangle_{i+\frac{1}{2},j} - \frac{1}{24} \left(\langle f \rangle_{i+\frac{1}{2},j+1} - 2 \langle f \rangle_{i+\frac{1}{2},j} + \langle f \rangle_{i+\frac{1}{2},j-1} \right) \right). \tag{25}$$

The point values $f_{i+\frac{1}{2},j}$ and $[v_r]_j$ are then used to evaluate the face-integrated flux, such that

$$\langle F \rangle_{i+\frac{1}{2},j} = r_{i+\frac{1}{2}} [v_r]_j f_{i+\frac{1}{2},j} h_\xi + \frac{1}{24} \left([v_r]_{j+1} \langle f \rangle_{i+\frac{1}{2},j+1} - 2 [v_r]_j \langle f \rangle_{i+\frac{1}{2},j} + [v_r]_{j-1} \langle f \rangle_{i+\frac{1}{2},j-1} \right). \tag{26}$$

Note that the flux evaluation requires accounting for the Jacobian r at the appropriate face because cell volumes increase along the radial direction. Combined with the interpolation step, Eqs. (24) and (26) prescribe a means of computing fourth-order fluxes from discrete cell-integrated values of the distribution function. The finite-volume formalism extends directly to three or more phase space dimensions by evaluating additional flux terms, and also including additional derivative terms along transverse directions and additional factors of cell spacing, as prescribed by the quadrature rule in Eq. (16).

3.3. Boundary condition implementation

The interpolation and fourth-order evaluation steps outlined in Secs. 3.1 and 3.2 for computing fluxes apply for cells that have neighbors. For cells at domain boundaries, the finite-volume flux evaluation can be handled through ghost cells or through one-sided reconstructions. For the boundary condition implementation used here, the interpolation procedure is modified and the fourth-order quadrature evaluation is left unchanged.

The specular reflection boundary condition (see Eq. (11)) on the distribution function is applied at the axis boundary and the wall boundary. Unlike typical Neumann and Dirichlet boundary conditions, the specular reflection boundary condition on the distribution function requires non-local information. For example, for the axis boundary in (r, v_r, v_θ) cylindrical phase space coordinates, the specular reflection condition is

$$f(r, v_r, v_\theta)|_{r=0} = f(r, -v_r, v_\theta)|_{r=0} \qquad \text{for } v_r > 0, \tag{27}$$

which requires information from $v_r < 0$ to set the boundary condition for $v_r > 0$. Since velocity components that are parallel to a specular-reflection boundary do not play a role when it comes to setting the boundary condition, the implementation discussion is limited to the two-dimensional (r, v_r) plane.

Let the radius be indexed by $i = \{0, 1, 2, \cdots, N_r - 1\}$ and let the velocity coordinate be indexed by $j = \{0, 1, 2, \cdots, N_{v_r} - 1\}$. See Fig. 2 for an illustration of the (r, v_r) plane and the associated indexing. For cylindrical phase space coordinates (r, v_r), specular reflection is implemented through an extrapolation procedure and a copy operation. This is done as follows. At the axis, for $j = \left\{ 0, 1, \cdots, \frac{N_{v_r}}{2} - 1 \right\}$, corresponding to $v_r < 0$

1. Use cells $i = \{0, 1, 2, 3, 4\}$ to perform a one-dimensional extrapolation, using a fifth-order accurate polynomial reconstruction to obtain the boundary value $\langle f \rangle_{-\frac{1}{2},j}$, such that

$$\langle f \rangle_{-\frac{1}{2},j} = \frac{1}{1800 h_r^2} \left(12019 \langle f \rangle_{0,j} - 5981 \langle f \rangle_{1,j} + 3019 \langle f \rangle_{2,j} - 981 \langle f \rangle_{3,j} + 144 \langle f \rangle_{4,j} \right) \tag{28}$$
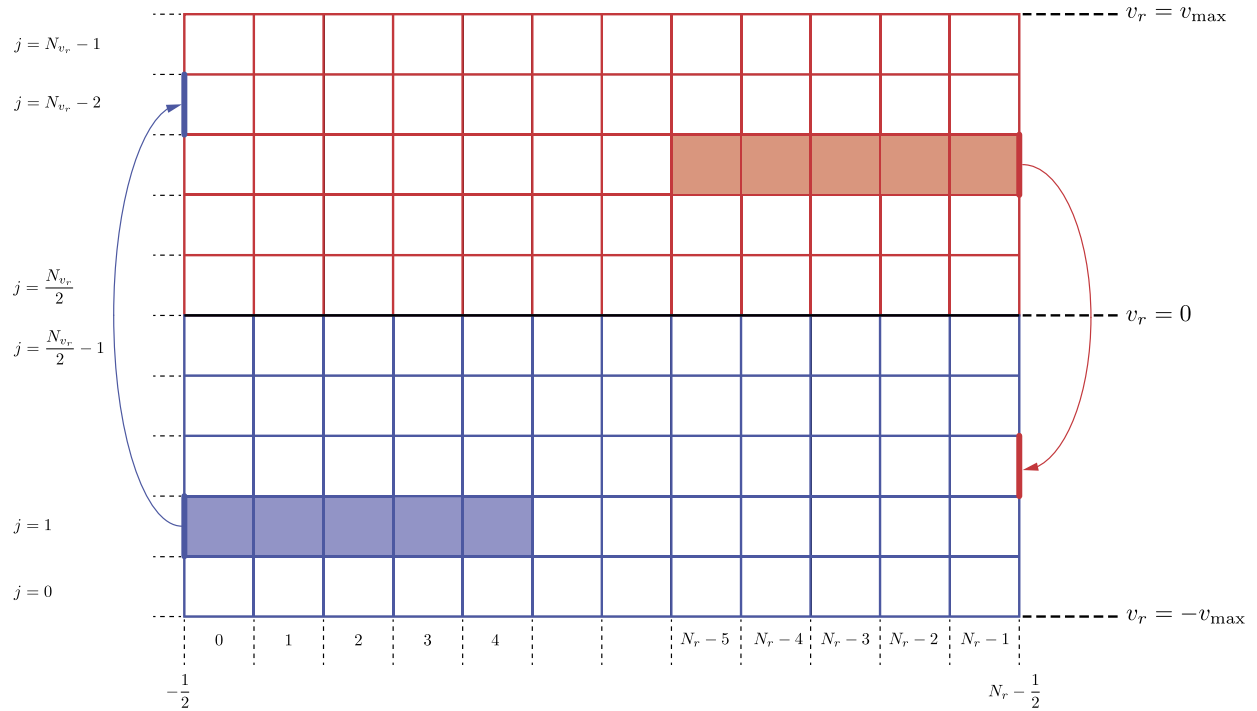
Fig. 2. Illustration of specular reflection boundary condition implementation for cylindrical (r, v_r) phase space coordinates at the left $(r = 0)$ axis boundary and at the right conducting wall boundary for $N_r = 12$ and $N_{v_r} = 10$. The red grid denotes $v_r > 0$, and the blue grid denotes $v_r < 0$. At the axis boundary, for each j in the lower half-plane a fifth-order accurate one-dimensional polynomial reconstruction is performed using five cells to extrapolate the distribution function value to the $i = -\frac{1}{2}$ face (thick blue line). This extrapolated value is then copied (blue arrow) to the corresponding cell face in the upper half-plane. Similarly, at the right conducting wall boundary, for each j in the upper half-plane, a fifth-order accurate one-dimensional polynomial reconstruction is performed using five cells to extrapolate the distribution function value to the $i = N_r - \frac{1}{2}$ face (thick red line). This extrapolated value is then copied (red arrow) to the corresponding cell face in the lower half-plane. (For interpretation of the colors in the figure(s), the reader is referred to the web version of this article.)

2. Copy value of $\langle f \rangle_{-\frac{1}{2}, j}$ to $\langle f \rangle_{-\frac{1}{2}, N_{v_r} - j - 1}$.

At the $r = r_{\max}$ wall boundary, for $j = \left\{ \frac{N_{v_r}}{2}, \frac{N_{v_r}}{2} + 1, \cdots, N_{v_r} - 1 \right\}$, corresponding to $v_r > 0$

1. Use cells $i = \{N_r - 5, N_r - 4, N_r - 3, N_r - 2, N_r - 1\}$ to perform a one-dimensional extrapolation using fifth-order accurate polynomial reconstruction to obtain the boundary value $\langle f \rangle_{N_r - \frac{1}{2}, j}$, such that

$$
\langle f \rangle_{N_r - \frac{1}{2}, j} = \frac{1}{60 h_r^2 (2N_r - 5)(24 + (N_r - 5)N_r(20 + 3(N_r - 5)N_r))} \Big(
$$
$$
\Big(\quad 576 \;-\; 1800 N_r \;+\; 1680 N_r^2 \;-\; 600 N_r^3 \;+\; 72 N_r^4\Big) \langle f \rangle_{N_r - 5, j}
$$
$$
+ \Big(\; -3924 \;+\; 11925 N_r \;-\; 10620 N_r^2 \;+\; 3525 N_r^3 \;-\; 378 N_r^4\Big) \langle f \rangle_{N_r - 4, j}
$$
$$
+ \Big(\; 12076 \;-\; 34875 N_r \;+\; 28580 N_r^2 \;-\; 8475 N_r^3 \;+\; 822 N_r^4\Big) \langle f \rangle_{N_r - 3, j}
$$
$$
+ \Big(-23924 \;+\; 61425 N_r \;-\; 42220 N_r^2 \;+\; 11025 N_r^3 \;-\; 978 N_r^4\Big) \langle f \rangle_{N_r - 2, j}
$$
$$
+ \Big(\; 48076 \;-\; 77175 N_r \;+\; 42980 N_r^2 \;-\; 9975 N_r^3 \;+\; 822 N_r^4\Big) \langle f \rangle_{N_r - 1, j} \Big)
$$

(29)

2. Copy value of $\langle f \rangle_{N_r - \frac{1}{2}, j}$ to $\langle f \rangle_{N_r - \frac{1}{2}, N_{v_r} - j - 1}$.

This procedure is illustrated in Fig. 2. The resulting values at the radial boundaries can then be used to evaluate fluxes, in accordance with the steps outlined in Sec. 3.2. Note that at $r = 0$ the radially-directed face-integrated flux is zero since the area associated with this cell face is zero; however, for the fourth-order discretization used here, the values $\langle f \rangle_{-\frac{1}{2}, j}$ are needed to perform a fifth-order accurate boundary-condition-informed reconstruction of the distribution function at the $(\frac{1}{2}, j)$ and $(\frac{3}{2}, j)$ faces. At these faces, the interpolation procedure described in Sec. 3.1 is modified to use $\langle f \rangle_{i, j}$ in the first four cells $(i = 0, 1, 2, 3)$ and the boundary value $\langle f \rangle_{-\frac{1}{2}, j}$ to perform the fifth-order accurate reconstruction. At $r = r_{\max}$

the radially-directed flux is non-zero, consequently the boundary values $\langle f \rangle_{N_r - \frac{1}{2}, j}$ are used to compute the flux at index $(N_r - \frac{1}{2}, j)$ and also to interpolate the distribution function to index $(N_r - \frac{3}{2}, j)$ and $(N_r - \frac{5}{2}, j)$.

As an aside, one can make an argument that much of the complexity associated with the cylindrical coordinate flux evaluations can be eliminated by evolving a volume-integral of the quantity rf with volume defined as in Cartesian coordinates ($dV = dr d\theta dz dv_r dv_\theta dv_z$) rather than evolving the volume-integral of the distribution function f with volume defined as in cylindrical coordinates ($dV = r dr d\theta dz dv_r dv_\theta dv_z$). Analytically the two formulations are equivalent, but numerically they amount to different discretizations. The latter approach is used here because the specular reflection axis boundary condition can be applied directly to the primary variable f, whereas in the case of rf being evolved as a primary variable, the axis boundary condition would have to be applied to an auxiliary variable f since the Jacobian is singular at the axis.

3.4. CFL stability condition on time step size

Discrete solvers for hyperbolic partial differential equations are subject to the Courant–Friedrichs–Lewy (CFL) condition, which stipulates an upper bound on the time step size. The time step size for the discretization used here is subject to the constraint

$$\Delta t \leq \sigma \cdot \min \left\{ \frac{h_r}{v_r}, \frac{h_\theta}{v_\theta}, \frac{h_z}{v_z}, \frac{h_{v_r}}{a_r + \frac{v_\theta^2}{r}}, \frac{h_{v_\theta}}{a_\theta - \frac{v_r v_\theta}{r}}, \frac{h_{v_z}}{a_z} \right\}, \tag{30}$$

where σ is the dimensionless Courant number and h_d is the cell spacing along the d-th direction. For RK4 time advance and fifth-order accurate upwind reconstructions a conservative upper bound on σ is $1.73/D$ [84], where D is the number of dimensions being discretized. This bound is derived assuming constant coefficient advection and ignores transverse derivative terms in the flux evaluation. For the Vlasov–Poisson simulations described here, it is found that using σ as high as 0.82 results in stable solutions.

Since velocities are coordinates in phase space, the maximum values of $\{v_r, v_\theta, v_z\}$ are set by the location of velocity domain boundaries for a given species. In the case of cylindrical coordinates, the Lorentz, centrifugal (v_θ^2/r), and Coriolis ($v_r v_\theta/r$) acceleration terms dictate the maximum advection speed along the velocity coordinates. The latter two present particularly stringent constraints on the time step size. For simulations that include the axis as part of the domain, the minimum value of the radius used to evaluate advection speed in the finite-volume discretization is $h_r/2$. This means that the centrifugal and Coriolis terms can have a value as high as $2v_{\max}^2/h_r$. Higher resolution along the radial direction thereby results in a higher value of the advection speed along v_r and v_θ directions, which further limits the time step size.

3.5. Poisson solver for electrostatic field in one dimension

In one spatial dimension the electric field can be computed either from Gauss's law or from Poisson's equation using the electrostatic potential. Here the latter approach is used. Integrating the Poisson equation (see Eq. (8)) over a one-dimensional volume and applying the divergence theorem yields the relation between the cell-integrated charge density (i.e. the total charge in a cell) $\langle \rho \rangle_i$ and the potential ϕ, such that

$$\langle \rho \rangle_i = - \left(\left[\frac{d\phi}{dr} \right]_{i+\frac{1}{2}} r_{i+\frac{1}{2}} - \left[\frac{d\phi}{dr} \right]_{i-\frac{1}{2}} r_{i-\frac{1}{2}} \right). \tag{31}$$

The point value of the derivative of the potential can be evaluated at a cell face using a fourth-order accurate finite-difference stencil, which can be derived using a fifth-order accurate polynomial reconstruction, such that

$$\left[\frac{d\phi}{dr} \right]_{i+\frac{1}{2}} = \frac{27}{24 h_r} (\phi_{i+1} - \phi_i) - \frac{1}{24 h_r} (\phi_{i+2} - \phi_{i-1}). \tag{32}$$

Using Eq. (32) to evaluate derivatives at the $i \pm \frac{1}{2}$ cell faces, substituting the result into Eq. (31), and grouping like indices yields the following relation between the discrete cell-integrated charge density and the cell-centered values of the electrostatic potential

$$\langle \rho \rangle_i = -\frac{1}{24 h_r} \left(-r_{i-\frac{1}{2}} \phi_{i-2} + \left(27 r_{i-\frac{1}{2}} + r_{i+\frac{1}{2}} \right) \phi_{i-1} - \left(27 r_{i-\frac{1}{2}} + 27 r_{i+\frac{1}{2}} \right) \phi_i \right.$$

$$\left. + \left(r_{i-\frac{1}{2}} + 27 r_{i+\frac{1}{2}} \right) \phi_{i+1} - r_{i+\frac{1}{2}} \phi_{i+2} \right). \tag{33}$$

At boundaries the stencils in Eq. (32) and Eq. (33) are modified to use boundary condition information. By symmetry arguments the boundary condition at the axis for the radial electric field is $E_r = 0$, which means that the condition on the

potential is $\frac{\partial \phi}{\partial r} = 0$. An additional boundary condition is stipulated by setting a homogeneous Dirichlet value at the outer radius, such that $\phi(r_{\max}) = 0$. This boundary condition ensures that the Laplacian operator is not singular. The actual chosen value of $\phi(r_{\max})$ is arbitrary. These conditions are used to perform one-sided polynomial reconstructions for ϕ to arrive at modified stencils for $d\phi/dr$ at boundaries. Thereby the stencils for the Poisson equation near boundaries are

$$\langle \rho \rangle_0 = -\frac{1}{24h_r}\left[-26\phi_0 r_{\frac{1}{2}} + 27r_{\frac{1}{2}}\phi_1 - r_{\frac{1}{2}}\phi_2 \right] \tag{34}$$

$$\langle \rho \rangle_1 = -\frac{1}{24h_r}\left[\left(26r_{\frac{1}{2}} + r_{\frac{3}{2}}\right)\phi_0 - \left(27r_{\frac{1}{2}} + 27r_{\frac{3}{2}}\right)\phi_1 + \left(r_{\frac{1}{2}} + 27r_{\frac{3}{2}}\right)\phi_2 - r_{\frac{3}{2}}\phi_3 \right] \tag{35}$$

$$\langle \rho \rangle_{N_r-1} = -\frac{1}{840h_r}\left[\left(5r_{N_r-\frac{3}{2}} + 75r_{N_r-\frac{1}{2}}\right)\phi_{N_r-4} - \left(63r_{N_r-\frac{3}{2}} + 441r_{N_r-\frac{1}{2}}\right)\phi_{N_r-3} \right.$$
$$\left. + \left(1015r_{N_r-\frac{3}{2}} + 1225r_{N_r-\frac{1}{2}}\right)\phi_{N_r-2} - \left(1085r_{N_r-\frac{3}{2}} + 3675r_{N_r-\frac{1}{2}}\right)\phi_{N_r-1} \right] \tag{36}$$

$$\langle \rho \rangle_{N_r-2} = -\frac{1}{840h_r}\left[-\left(35r_{N_r-\frac{5}{2}} + 5r_{N_r-\frac{3}{2}}\right)\phi_{N_r-4} + \left(945r_{N_r-\frac{5}{2}} + 63r_{N_r-\frac{3}{2}}\right)\phi_{N_r-3} \right.$$
$$\left. - \left(945r_{N_r-\frac{5}{2}} + 1015r_{N_r-\frac{3}{2}}\right)\phi_{N_r-2} + \left(35r_{N_r-\frac{5}{2}} + 1085r_{N_r-\frac{3}{2}}\right)\phi_{N_r-1} \right]. \tag{37}$$

Note that $r_{\frac{1}{2}} = h_r$, $r_{\frac{3}{2}} = 2h_r$, $r_{N_r-\frac{1}{2}} = r_{\max}$, $r_{N_r-\frac{3}{2}} = (r_{\max} - h_r)$, $r_{N_r-\frac{5}{2}} = (r_{\max} - 2h_r)$. Equations (33) to (37) are used to construct a linear system with the full discrete Laplacian operator matrix stored in memory. The equation system is solved using the iterative stabilized biconjugate gradient method with tolerance set to 10^{-16}, which corresponds to the relative residual error. Note that the Laplacian operator matrix is not symmetric, which is often the case for finite-volume discretizations of elliptic equations with variable coefficients and/or non-periodic boundary conditions [85–87]. From point values of the electrostatic potential, the point values of the electric field can be derived using a fifth-order polynomial reconstruction of ϕ, which can either be centered,

$$(E_r)_i = -\frac{1}{12h_r}\left(\phi_{i-2} - 8\phi_{i-1} + 8\phi_{i+1} - \phi_{i+2} \right), \tag{38}$$

or one-sided for cells near boundaries. The use of point values both for the potential and electric field circumvents the need for radially-weighted polynomial reconstructions for ϕ and also ensures more straightforward evaluation of fluxes using the quadrature rule in Eq. (16). Note that if a given system has a net zero charge, then by Gauss's law E_r will be zero at $r_{\max}$ and will remain zero as a result of conservation (since the integral of the distribution function is conserved, so is the total charge) and the reflecting wall boundary condition, which ensures that charge cannot leave the system. Thereby, for physical fidelity it is not necessary to explicitly set a boundary condition on E_r at $r_{\max}$.

3.6. Algorithm outline

The algorithm outline for solving the Vlasov–Poisson equation system in cylindrical phase space coordinates is as follows. The distribution function is initialized as a fourth-order volume-integrated value in each phase space cell using either analytic definite integrals or a quadrature rule, and the following steps are performed within each stage of the RK4 time integration:

1. Compute charge density from the zeroth velocity moment of the distribution functions.
2. Solve the Poisson equation for the discrete potential (see Sec. 3.5).
3. Compute the electric field from the discrete values of the potential using either centered stencils (see Eq. (38)) or one-sided stencils near boundaries.
4. Interpolate the cell-integrated distribution function to cell faces using an upwinded stencil, derived in Sec. 3.1.
5. Compute the face-integrated fluxes using the fourth-order quadrature rule described in Sec. 3.2.
6. Compute the righthand side of Eq. (12) to obtain the RK4 k-th stage increment to the distribution function.

The distribution function is then updated using the increments obtained from each stage of RK4.
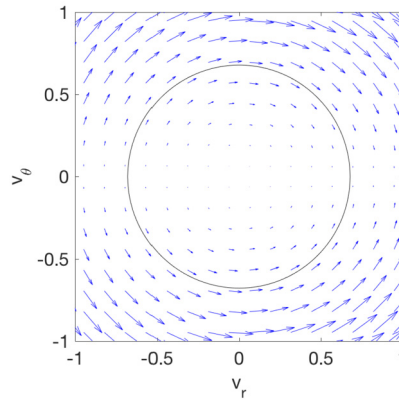
Fig. 3. The circulation pattern in (v_r, v_θ) plane due to the centrifugal (v_θ^2/r) and Coriolis $(-v_r v_\theta/r)$ terms in the cylindrical coordinate Vlasov equation. Arrows indicate the direction of advection and the black circle is drawn for reference to better show the circular flow pattern.

4. Axisymmetric simulations in cylindrical phase space coordinates

While there have been extensive developments in the finite-volume discretization of the Euler and Navier–Stokes equations in axisymmetric geometries [88,89], the features of the axis singularity are distinctly different in these equation systems compared to the Vlasov equation. In particular, since velocities are coordinates in the Vlasov equation, the regularity condition often applied in fluid calculations (i.e. the condition that radial velocity is linearly dependent on radius as $r \to 0$) does not apply. Conservative discretization of the continuum kinetic cylindrical coordinate Vlasov equation thereby constitutes largely uncharted territory. Here the fourth-order finite-volume discretization is applied to a uniform neutral gas to investigate convergence properties of the algorithm. The numerical method is then applied to an electrostatic Z-pinch configuration to study the kinetic physics of an axisymmetric plasma.

4.1. Preservation of a spatially uniform neutral gas distribution function

A unique aspect of cylindrical phase space coordinates is that the distribution function always advects in velocity space due to Coriolis and centrifugal force terms (see Fig. 3), which are present whenever the radial direction is involved. This feature, combined with the fact that in the absence of collisions a perturbed Vlasov equilibrium cannot return to the original state, has important implications.

Consider the case of a one-dimensional spatially-uniform thermal-equilibrium neutral gas, such that the Lorentz acceleration terms are zero. In Cartesian phase space coordinates this equilibrium is maintained as long as the associated numerical method can preserve zero-gradient solutions. By contrast, for a spatially uniform equilibrium state to be preserved in cylindrical coordinates (i.e. for $\partial f/\partial t$ to be zero) multiple non-zero terms in the Vlasov equation have to cancel each other exactly. In conservative form (Eqs. (5) and (10)) the r, v_r, and v_θ derivative terms must all cancel each other. For example, setting f to be a Maxwellian distribution function (see Eq. (39)) that is spatially uniform and evaluating the terms in Eq. (5), one can show that $\partial f/\partial t$ is indeed zero. While this cancellation is analytically exact, it is not necessarily exact in the discrete form of the Vlasov equation. This means that in cylindrical phase space coordinates numerical error alone can cause a spatially-uniform distribution function to evolve away from equilibrium.

Even if it cannot exactly preserve a spatially-uniform equilibrium state, a robust numerical method must converge to the initialized equilibrium solution as the grid is refined. Here it is demonstrated that for a function initialized to an equilibrium and integrated forward in time using the fourth-order finite-volume discretization described in Sec. 3, the change in the distribution function $\partial f/\partial t$ is not zero, but converges to zero at the expected rate as the grid is refined.

Let f_0 be defined in (r, v_r, v_θ) coordinates as a spatially-uniform Maxwellian distribution function, such that

$$f_0 = \frac{A}{2\pi v_T^2} \exp\left(-\frac{v_r^2 + v_\theta^2}{2v_T^2}\right), \tag{39}$$

where A is a scalar factor and v_T is the thermal speed. Note that it can be shown through coordinate transformation that Eq. (39) is equivalent to a Maxwellian in Cartesian (v_x, v_y) coordinates. This solution is advanced in time using Eq. (10) with Z_s set to zero and with $A = 1/8$, $v_T = 0.10$, $v_r, v_\theta \in [-1, 1] \times [-1, 1]$, and $r \in [0, 4]$. The value of $v_{\max}$ is chosen such that the distribution function is zero to machine precision at velocity boundaries for all simulated time. Results are presented in Figs. 4 to 6 for different grid resolutions. A fixed time step size of $\Delta t = 2 \times 10^{-4}$ is used in these simulations, such that CFL number $\sigma = \{0.20, 0.46, 0.82\}$ for resolutions 64^3, 96^3, and 128^3, respectively.

Fig. 4 shows the net change in mass, computed from the zeroth moment of the distribution function; the net change in the total volume-integrated momentum in the v_r and v_θ directions, computed from the first velocity moments of the
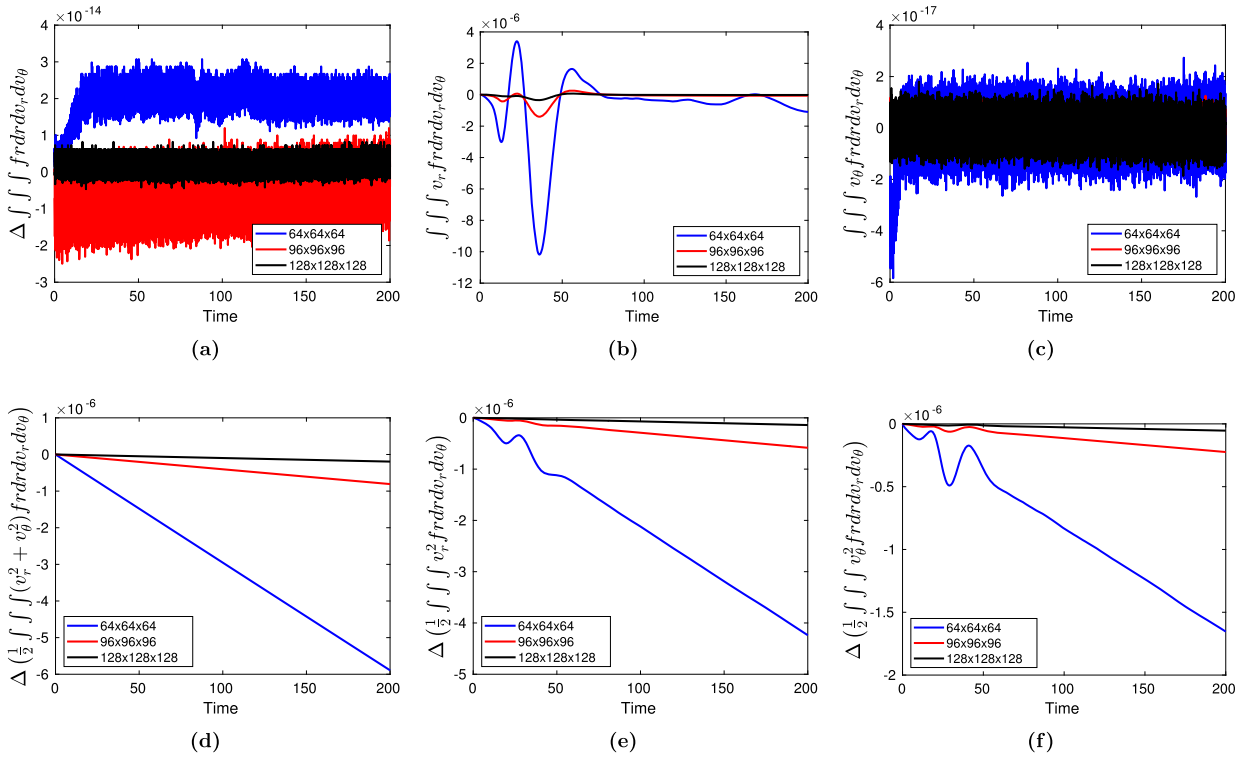
Fig. 4. Evolution of volume-integrated quantities derived from velocity moments of an initially uniform, zero-drift distribution function: (a) change in mass relative to initial value of one; (c) radial momentum; (b) azimuthal momentum; (d) change in total kinetic energy; (e) change in kinetic energy associated with radial motion, relative to initial value of 5.0×10^{-3}; and (f) change in kinetic energy associated with azimuthal motion, relative to an initial value of 5.0×10^{-3}. All moments are either conserved to machine precision or converge to initialized values as the grid is refined. For radial dynamics, the numerical errors affect both the v_r drift and the thermal kinetic energy associated with radial motion. For the azimuthal direction the numerical errors are associated exclusively with thermal kinetic energy, not drift.

distribution function; and the net change of the kinetic energy in the system, computed from the second velocity moment of the distribution function. The net change in mass is zero to numerical precision, independent of the resolution. This is guaranteed by the finite-volume discretization provided that the system boundaries are closed, which is ensured by specular reflection at radial boundaries and zero-flux boundaries at v_r, $v_\theta = \pm v_{max}$. The total volume-integrated value of the radial momentum decreases with time from an initial value of zero, indicating that the original Maxwellian distribution function develops a drift toward the axis. As the grid is refined, the magnitude of the drift decreases toward zero, leading to smaller departures away from equilibrium. The value of the net azimuthal momentum stays fixed at zero for all time, indicating that numerical errors do not impart any rotation on the neutral gas represented by the distribution function. The total kinetic energy decreases with time from an initial value of 1.0×10^{-2}, and the net change in the kinetic energy shrinks as grid resolution is increased, which is the expected result for a convergent algorithm.

Fig. 5 shows the evolution of the net change in density and radial momentum as function of radius and time. For an equilibrium system, the net change should be zero, but due to numerical errors spatial variations develop at the axis and at the r_{max} boundary. These arise due to the inability of the numerical method to exactly preserve the isotropic velocity dependence of the Maxwellian distribution function. The departure from a Maxwellian leads to a lack of cancellation of the terms in Eq. (10) and results in advection along the radial direction. The most significant departure from the equilibrium initial condition occurs at the axis where the advection speeds are largest. These features start off as localized spikes and then propagate into the domain, amplifying in time. The features amplify until they become on the order of the truncation error, at which point they are subject to numerical dissipation from the upwind spatial discretization, which smooths out these variations in cells that are at least $3h_r$ away from the radial boundaries. As the grid resolution is increased, the variations converge to zero at the expected rate for a fourth-order discretization. In the context of a plasma, density features would lead to the generation of electric fields, which would result in more complicated dynamics induced by numerical errors and the ensuing departure from equilibrium.

Since analytically the net change in the solution should be zero, the convergence rate can be computed from 64^3 and 128^3 resolution simulations. The convergence rate p is computed using the L_1-norm, such that for a discrete solution u^N on a grid with N cells along each direction,
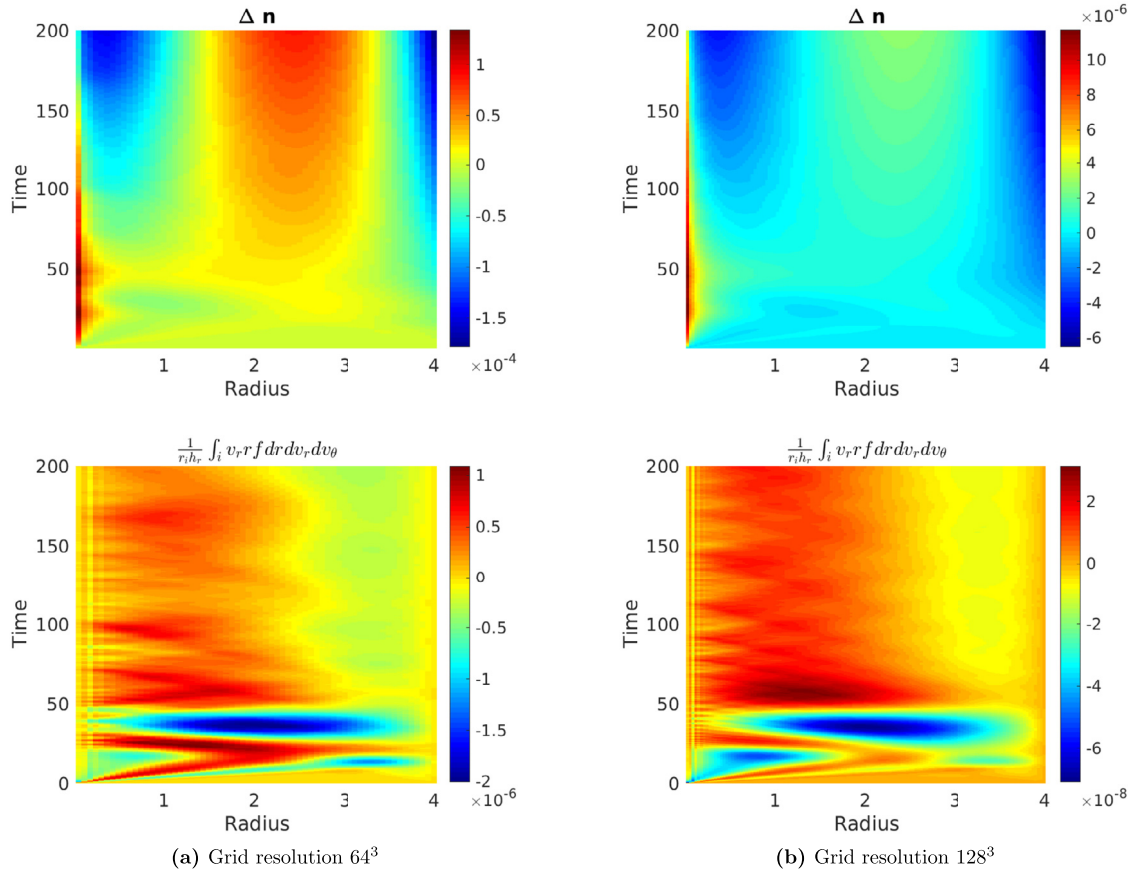
Fig. 5. Evolution of the change in number density (top) and radial momentum (bottom) for a spatially-uniform Maxwellian initial condition using (a) 64^3 resolution and (b) 128^3 resolution grids. Spike features arise at domain boundaries due to numerical errors and amplify in time until they are subject to dissipation by the upwind discretization, which causes them to smooth out into larger-wavelength numerical features. As the resolution is doubled the variations diminish by a factor of about fifteen for density and a factor of about twenty-five for momentum.

$$p = \frac{1}{\log 2} \log \left(\frac{\|u^N - u^N_{exact}\|_1}{\|u^{2N} - u^{2N}_{exact}\|_1} \right), \qquad \|u^N - u^N_{exact}\|_1 = \int_V |u^N - u^N_{exact}| dV, \tag{40}$$

where V is the volume of the domain on which the variable u is defined. Evaluating the convergence rate for number density at time $t = 10$ (time step 50,000) yields a convergence rate of 4.23. Additional quantitative assessment of the convergence rate is shown in Fig. 6 where the L_1-norm of the error for the distribution function and its moments are plotted as a function of grid spacing. Note that number density is a cell-averaged quantity, whereas the other moments are cell-integrated quantities. The electric field is zero in this neutral gas simulation, such that accuracy is not affected by the truncation error of the field solver. The distribution function converges at a rate of 4.7. Since time-discretization errors are much smaller than spatial-discretization errors, the convergence rate is expected to be between fourth and fifth order due to the combined use of fifth-order reconstructions and fourth-order flux evaluations [84]. Velocity moments of the distribution function likewise converge at a rate that is slightly higher than fourth-order.

Based on the results in Figs. 4 to 6 it is expected that as long as the magnitude of the physical dynamics of interest are well above truncation error for the duration of a simulation, then numerical errors associated with lack of cancellation are unlikely to overwhelm a physical solution. Since the algorithm demonstrably converges at fourth-order, a convergence study can elucidate the significance of these errors in any given problem setup. It is possible that the discretization of the Vlasov equation can be modified so as to eliminate cancellation errors entirely. For example, for neutral gas dynamics, one can treat the (v_r, v_θ) plane as being in polar coordinates [63,64,60] and thereby take advantage of the fact that characteristics are circles in this plane (see Fig. 3). For plasmas, however, the presence of a radial or azimuthal Lorentz acceleration in the Vlasov equation breaks this circular symmetry. Further characterization of these errors and possible means of addressing them are left as a topic for future research.

Investigating the behavior of the solution in a steady-state configuration yields insights into the numerical solutions obtained for dynamic problems. Here it is demonstrated that the finite-volume solution (a) converges to the expected steady-state value and (b) converges at the expected rate when applied to model an equilibrium. Verified convergence
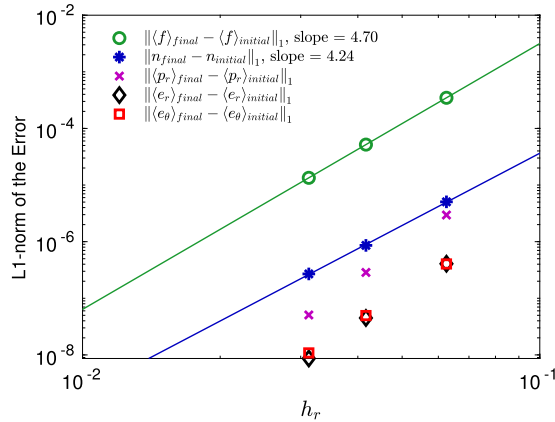
Fig. 6. Convergence of the L_1-norm of the error at time $t = 10$ (time step 50,000, $\Delta t = 2 \times 10^{-4}$) in simulations of a uniform neutral gas in (r, v_r, v_θ) coordinates using resolutions $64^3, 96^3, 128^3$. Shown are the L_1-norms for the distribution function f, number density n, radial momentum p_r, kinetic energy associated with radial motion e_r, and kinetic energy associated with azimuthal motion e_θ. All quantities converge at or slightly above fourth order because the dominant error is due to the spatial discretization, which uses fifth-order reconstructions and fourth-order quadratures.

yields confidence that in the limit of infinite resolution the approximate numerical solution approaches the true solution to the governing partial differential equation.

4.2. Ion confinement in a one-dimensional Z-pinch

The cylindrical coordinate Vlasov–Poisson solver described here is designed to study kinetic effects in axisymmetric plasmas. A one-dimensional plasma configuration is considered – that of the Z-pinch. Z-pinches feature a simple cylindrical geometry and rapid onset of instabilities, meaning they have fast dynamics that are accessible to kinetic simulations. Computational investigation of Z-pinch dynamics are typically carried out using fluid models; however, kinetic effects are believed to be important, particularly near the axis where the mean free path and Larmor radius can be large relative to the system size [90] and also in regions of large density gradients, which can lead to drift wave turbulence [91].

In a Z-pinch, electrons carry the bulk of the current, and are thereby electromagnetically confined, whereas ions, which carry little current, are electrostatically confined. The objective here is to model this collisionless configuration along the radial direction, with ion dynamics modeled in (r, v_r, v_θ) phase space coordinates, and electron distribution assumed to be fixed for all time. In an equilibrium setting this system can be described by the two-fluid model, such that ion pressure is balanced by the electric field

$$\frac{\partial P_i}{\partial r} = q_i n_i E_r \tag{41}$$

and electron pressure is balanced by the electric and magnetic field,

$$\frac{\partial P_e}{\partial r} = q_e n_e \left(E_r - u_{ze} B_\theta \right). \tag{42}$$

Assuming that electrons are stationary means physically that the electron density and pressure gradient are constant for all time, which implies that any change in E_r is exactly balanced by a change in the $u_{ze} B_\theta$ term on time scales that are much faster than ion dynamics. In effect, due to their negligible inertia, electrons are assumed to act as a fixed non-uniform background.

To study ion dynamics, the ions are initialized to be radially displaced from the electrons, such that the ions are not in equilibrium with the electron profile – see Fig. 7. The resulting electric field accelerates the ions toward the stationary electrons, and thereby the initial potential energy is converted into kinetic energy. The ions move toward the axis until they overshoot the electrons, causing the electric field to change sign and to accelerate the ions radially outward, and the process repeats. For small perturbations, this type of electrostatic oscillation is known as a Langmuir wave, and is well-characterized in the context of a spatially-uniform plasma, where the frequency as a function of wavelength of perturbation is prescribed by the Bohm–Gross dispersion relation derived from linear theory [92]. This dispersion relation, however, does not hold for large deviations from equilibrium and does not apply for the case of an axisymmetric Z-pinch because the plasma pressure is not uniform such that the plasma frequency and thermal speed can vary spatially. Moreover, in the kinetic model description, phase mixing also plays a role, such that the oscillation is nonlinear and can damp in time through mechanisms like Landau damping.

For the computational investigation of this problem, the ions and electrons are initialized to have a smooth radial profile with compact support, such that the densities are
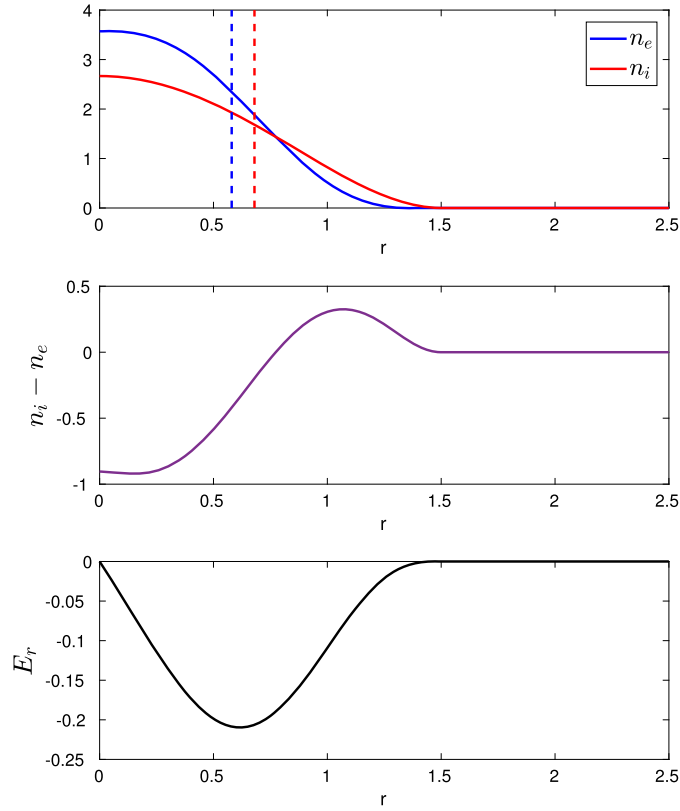
Fig. 7. Initial conditions for simulation of electrostatic ion confinement in cylindrical phase space coordinates. The plots show: ion density and electron density (top) with the mean radius – defined in Eq. (45) – indicated by dashed lines; charge density (middle); and the associated electric field (bottom). Electrons are assumed to be stationary, such that only the ions evolve.

$$n_i(r) = \frac{8}{3}\left(1 - \frac{8}{9}r^2 + \frac{16}{81}r^4\right) \qquad\qquad r \in [0, r_{0,i}] \tag{43}$$

$$n_e(r) = \frac{250}{77}\left(\frac{11}{10} - \frac{1375}{343}r^3 + \frac{20625}{4802}r^4 - \frac{20625}{16807}r^5\right) \qquad r \in [0, r_{0,e}] \tag{44}$$

where $r_{0,i} = 1.5$ and $r_{0,e} = 1.4$. These polynomials satisfy the following constraints: for electrons $\int_0^{r_{0,e}} n_e r\,dr = 1$, $n_e'(0) = 0$, $n_e(r_{0,e}) = 0$, $n_e'(r_{0,e}) = 0$ and for ions $\int_0^{r_{0,i}} n_i r\,dr = 1$, $n_i'(0) = 0$, $n_i'(r_{0,i}) = 0$. The constraints on derivatives are meant to ensure smoothness and are not strictly necessary, but are helpful in the context of high-order discretizations when limiters are not used. Note that the density profiles are scaled so that the total ion charge in the system is one and the net charge is zero. The ion velocity dependence is an isotropic zero-drift Maxwellian (Eq. (39) with $A = 1$) with thermal speed $v_T = 0.10$, such that the temperature is spatially uniform. Since the electrons are assumed to be stationary their velocity dependence is of no consequence. The mean radius for each species can be evaluated using the expression

$$\bar{r}_s = \frac{\int_0^{r_{max}} n_s r^2 dr}{\int_0^{r_{max}} n_s r\,dr}, \tag{45}$$

such that $\bar{r}_e \approx 0.583$ for all time and $\bar{r}_i \approx 0.686$ at initial time. The mean radius indicates the average radial location of each species, and thereby provides a metric for evaluating the distance between the ion and electron distributions. The initial number densities, total charge density, and associated radial electric field, which can be derived from Gauss's law, are plotted in Fig. 7.

The non-dimensionalized governing equations for the ions in (r, v_r, v_θ) coordinates are given by Eqs. (8) and (10). The domain is $r, v_r, v_\theta \in [0, 4] \times [-1, 1] \times [-1, 1]$. To assess the convergence properties of the Vlasov–Poisson solver when the field solve and time advance are both included, the initial condition is evolved forward in time on 64^3, 128^3, and 256^3 grids for time $t \in [0, 1.5]$ using a time step size of $\Delta t = 4 \times 10^{-5}$. Richardson error estimation is used to compute the convergence rate for the cell-integrated distribution function, the cell-centered electrostatic potential, and the cell-centered electric field. The L_1-norm of the difference between distribution functions on a N^3 and a $(2N)^3$ grid is defined to be

Table 1
Convergence rate using Richardson error estimation at different snapshots in time for the simulation of axisymmetric ion confinement in a Z-pinch. A time step size of $\Delta t = 4 \times 10^{-5}$ is used for all grid resolutions (64^3, 128^3, and 256^3).

Time	Variable	$\|u^{64} - u^{128}\|_1$	$\|u^{128} - u^{256}\|_1$	Convergence rate p
$t = 0.5$	$\langle f \rangle$	5.2915e−04	4.3215e−05	3.61
	E_r	2.9275e−04	1.4589e−05	4.33
	ϕ	7.9670e−06	4.5031e−07	4.15
$t = 1.0$	$\langle f \rangle$	9.3633e−04	7.2006e−05	3.70
	E_r	2.9457e−04	1.5378e−05	4.26
	ϕ	8.1050e−06	4.6025e−07	4.14
$t = 1.5$	$\langle f \rangle$	1.3224e−03	9.8633e−05	3.75
	E_r	2.9569e−04	1.6369e−05	4.18
	ϕ	8.3592e−06	4.7798e−07	4.13

$$\|\langle f^N \rangle - \langle f^{2N} \rangle\|_1 = \sum_{i=1}^{N} \sum_{j=1}^{N} \sum_{k=1}^{N} \left| \langle f^N \rangle_{i,j,k} - \langle \tilde{f}^N \rangle_{i,j,k} \right| \tag{46}$$

where

$$\langle \tilde{f}^N \rangle_{i,j,k} = \sum_{i'=2i-1}^{2i} \sum_{j'=2j-1}^{2j} \sum_{k'=2k-1}^{2k} \langle f^{2N} \rangle_{i',j',k'}. \tag{47}$$

The L_1-norm of the difference between solutions u^N and u^{2N} defined at cell centers on two different grids is

$$\|u^N - u^{2N}\|_1 = \sum_{i=1}^{N} \left| u_i^N - \mathbb{P}_i(u^{2N}) \right|, \tag{48}$$

where $\mathbb{P}_i$ is an operator that denotes a high-order interpolation of the cell-centered solution on a given fine grid onto the cell centers (indexed by i) of the coarsest grid. To ensure that interpolation error is negligible compared to truncation error, this interpolation is chosen to be sixth-order accurate for ϕ and E_r. The ratio of norms yields an estimate of the convergence rate p, such that

$$p = \frac{1}{\log 2} \log \left(\frac{\|u^{2N} - u^N\|_1}{\|u^{4N} - u^{2N}\|_1} \right) \tag{49}$$

for the chosen refinement ratio of two. Table 1 shows the errors in the solution for two successive grid refinements and the associated convergence rate, which is consistently fourth-order. The largest errors for the distribution function are at $r = r_{0,i}$, where the initial density profile transitions from finite to zero. These localized errors diminish in time due to transport of ions to larger radii and due to numerical dissipation, which is why the convergence rate for the distribution function increases slightly as the solution evolves. Such errors can be reduced with smoother initial conditions and limiters, which are not explored here.

Long-time evolution of the distribution function $f(r, v_r, v_\theta)$, averaged over each cell, is shown in Fig. 8 for a 128^3 resolution grid. As the ions are accelerated toward the axis, the bulk of the distribution function shifts toward negative v_r, such that the magnitude of the shift is radius-dependent, which can be seen in the (r, v_r) plane. As the ions move toward the axis, they are compressed and heated, as evidenced by the distribution function widening in the (v_r, v_θ) plane, which corresponds to an increase in thermal speed. When the ions overshoot the electrons they are accelerated in the positive radial direction, such that the bulk of the distribution function shifts toward positive v_r. As the ions move away from the axis, they cool, resulting in a decrease in thermal energy seen by the narrowing of the distribution function in the (v_r, v_θ) plane. Since the density depends on radius, the amount of time that it takes for a portion of the distribution function to move from the $v_r < 0$ half-plane to the $v_r > 0$ half-plane is also radius-dependent. This results in a non-linear oscillation. Since the distribution function also moves along the radial direction, the oscillation is accompanied by phase mixing, and the development of substructures. The magnitude of the shifts in the v_r direction decreases in time, and ultimately the distribution function reaches an equilibrium-like state, as indicated by the diminished amplitude of the fluctuations.

The total integral of the ion distribution function in the system, and thereby the net mass and charge, is conserved to round-off error, as is guaranteed by the discretization. The evolution of the net ion momentum in the system is shown in Fig. 9 for grid resolutions 64^3, 96^3, and 128^3. A time step size of $\Delta t = 2 \times 10^{-4}$ is used for all three resolutions. The net momentum along the radial direction oscillates in time about zero, and the magnitude of the momentum approaches zero, indicating a transition to a state that is closer to equilibrium. Thus the bulk of the energy originally in the electric field is transferred into thermal energy, as opposed to directed kinetic energy. This behavior is consistent with the dynamics seen in the distribution function (see Fig. 8) from which the momentum is derived. The net azimuthal momentum in the system is zero to machine precision, as there are no forces (and no numerical errors) that induce rotation.
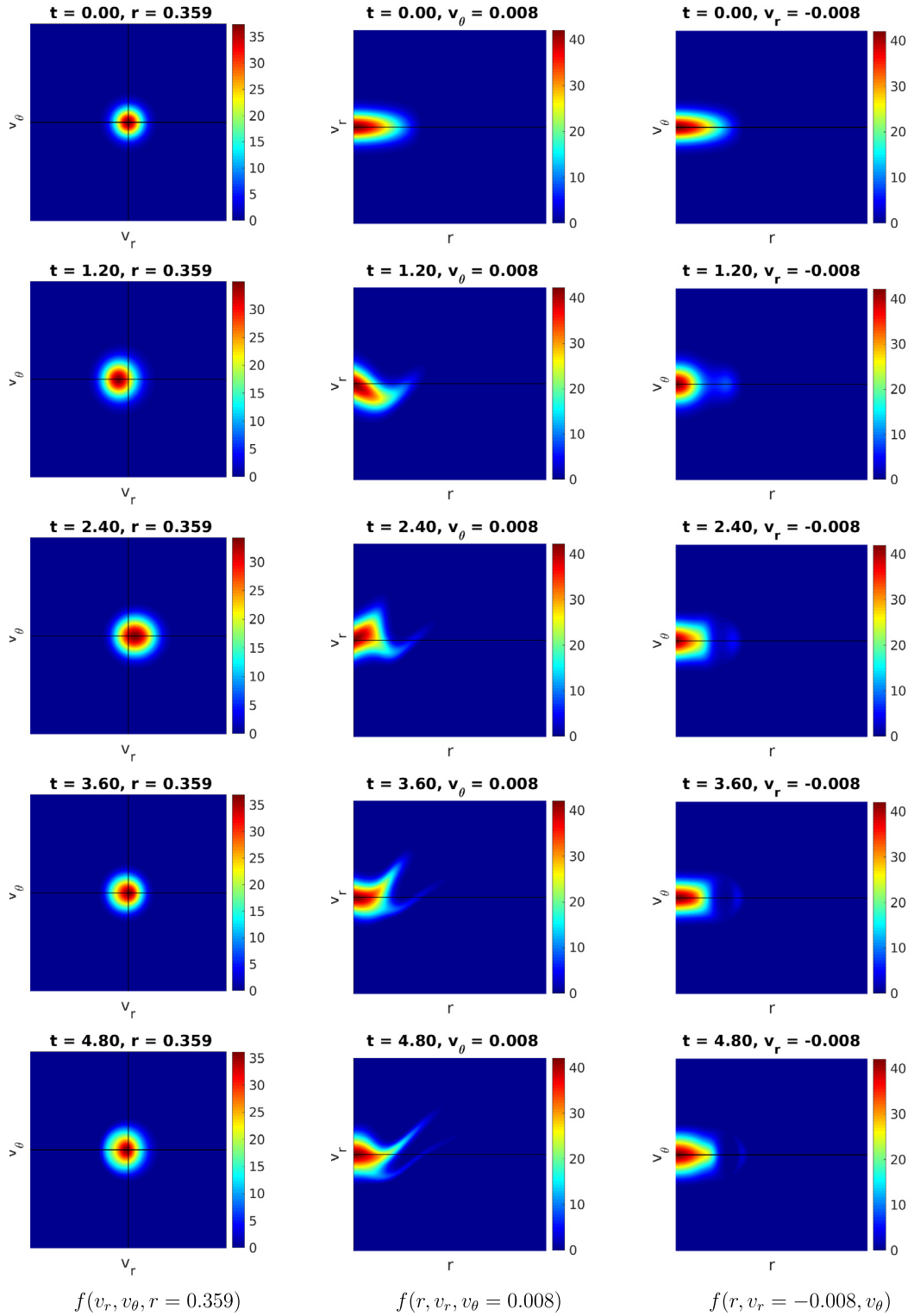
Fig. 8. Evolution of the cell-averaged distribution function $\frac{1}{r_i h_r h_{v_r} h_{v_\theta}} \langle f \rangle_{i,j,k}$ in different planes in phase space for 128^3 simulation of axisymmetric ion confinement in a Z-pinch. Non-Maxwellian features are observed as ions oscillate toward and away from the axis.
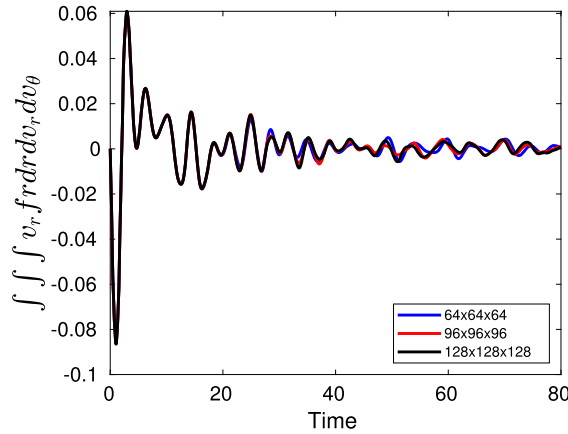
Fig. 9. Evolution of the net radial momentum in simulations of axisymmetric ion confinement in a Z-pinch. The radial momentum oscillates about zero as the ions move toward and away from the axis. Results from three different grid resolutions are shown, and indicate that the solution converges as the grid is refined.
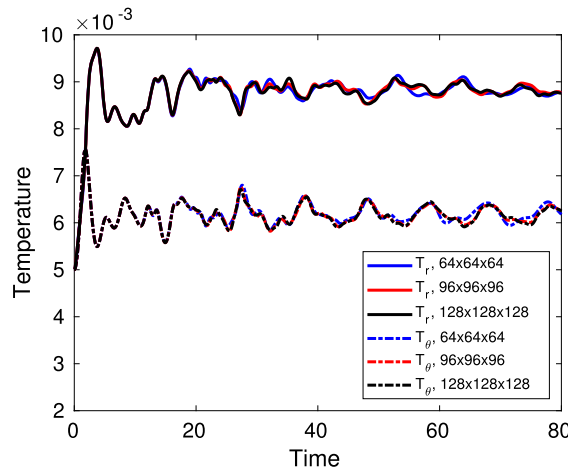

Fig. 10. Evolution of the net ion temperature associated with random motion along the radial direction (T_r) and random motion along the azimuthal direction (T_θ) in simulations of axisymmetric ion confinement in a Z-pinch. A temperature anisotropy develops such that $T_r > T_\theta$, and the temperatures oscillate in time. Results from three different grid resolutions are shown, and indicate that the solution converges as the grid is refined.

The evolution of the net temperature is shown in Fig. 10. The net temperature is computed from the moments of the distribution function, such that analytically the temperature associated with plasma motion along the d-th direction is the difference between total and directed kinetic energy along the d-th direction:

$$T_d = \frac{1}{2}\left[\frac{\int_0^{r_{max}}\int_{-\infty}^{\infty}\int_{-\infty}^{\infty} v_d^2 f dv_r dv_\theta r dr}{\int_0^{r_{max}}\int_{-\infty}^{\infty}\int_{-\infty}^{\infty} f dv_r dv_\theta r dr} - \left(\frac{\int_0^{r_{max}}\int_{-\infty}^{\infty}\int_{-\infty}^{\infty} v_d f dv_r dv_\theta r dr}{\int_0^{r_{max}}\int_{-\infty}^{\infty}\int_{-\infty}^{\infty} f dv_r dv_\theta r dr}\right)^2\right], \tag{50}$$

where a scalar factor of ion mass is omitted as it is in effect one in this non-dimensionalized setting. From simulation data, the integrals in Eq. (50) are performed over the computational domain to fourth-order accuracy using the fourth-order quadrature rule given in Eq. (16). A temperature anisotropy develops, such that the thermal energy associated with motion along the radial direction becomes greater than the thermal energy associated with motion along the azimuthal direction. Such anisotropy is expected since there are no collisions to drive the ions toward an isotropic distribution. The net gain in thermal energy comes at the expense of the potential energy, associated with the electric field.

The spatiotemporal evolution of ion number density is shown in Fig. 11. At time $t = 80$ the mean radius of the ions is 0.722, such that the separation between the ions and electrons is 0.138. This separation distance is on the order of a Debye length, which is the distance at which the dynamic species (in this case the ions) screens out the electric field of the stationary electrons. Notably the Debye length ($\lambda_D = v_T/\omega_{pi}$) does not have a single value in this system since plasma frequency is spatially dependent. As a point of comparison, the initial Debye length, using the initial condition thermal speed $v_T = 0.10$ and plasma frequency defined in terms of the average number density in the system, is $\lambda_D = 0.283$. Fig. 11
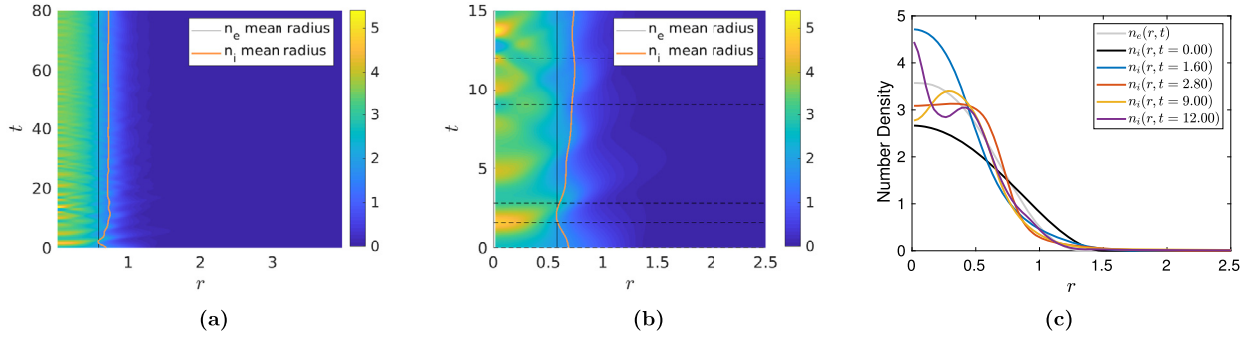
Fig. 11. (a) Evolution of ion number density as a function of position and time in a 128^3 resolution simulation of axisymmetric ion confinement in a Z-pinch. At time $t = 80$ the mean radius of the ions is 0.722, and the separation between ions and electrons is 0.138. (b) Ion number density evolution for $t \in [0, 15]$ and $r \in [0, 2.5]$, showing multimodal structures. Representative density profiles are shown in dashed lines and are plotted as a function of radius in (c).
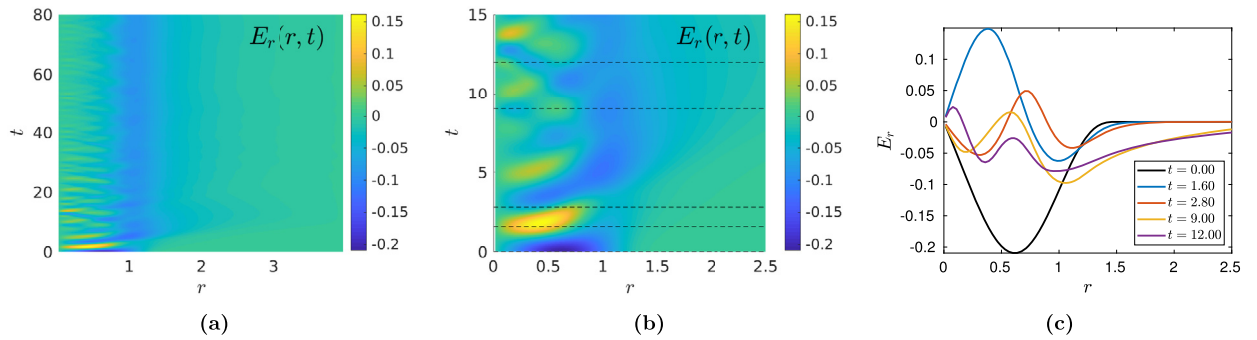
Fig. 12. (a) Evolution of the radial electric field as a function of position and time in a 128^3 resolution simulation of axisymmetric ion confinement in a Z-pinch. The electric field damps non-linearly as a function of time. A negative electric field, directed toward the axis, develops at the periphery of the ion density distribution and confines the ions to the stationary electrons. (b) Contour plot of the evolution of radial electric field for $t \in [0, 15]$ and $r \in [0, 2.5]$. Multimodal features appear throughout the evolution, and representative profiles are marked by dashed lines and are plotted as a function of radius in (c).

shows that the original monotonically-decreasing density profile later develops local minima and maxima, depending on the local motion of the ions. These profiles are consistent with the multi-modal structures in the electric field.

The electric field evolution for the ion confinement simulation is shown in Fig. 12. The electric field is initially negative (directed toward the axis) for $r \in [0, 1.5]$, and changes sign whenever ions overshoot the electrons as they move toward and away from the axis. The electric field magnitude decreases as a function of time, indicating that some of the original electric field energy is converted to kinetic energy. Unlike the initial condition (see Fig. 7), in which the electric field is localized, by the end of the simulation the electric field is non-zero throughout much of the domain. This means that ions have reached the $r = r_{\max}$ boundary. A negative electric field develops at the periphery of the bulk ion density distribution, confining the ions to the stationary electrons. The initial ion oscillation has a period of approximately π (as evidenced in the density contours shown in Fig. 11(b) and electric field contours shown in Fig. 12(b)), which corresponds to a frequency of two. This frequency is consistent with the Bohm–Gross dispersion relation in the low-temperature limit, which would predict an oscillation frequency of order unity for the plasma densities involved. The low-temperature approximation applies in this case since the initial thermal speed is $v_T = 0.10$ and perturbation wavenumber is of order unity. Ultimately, however, nonlinear dynamics dominate the solution, and the initial coherent oscillation gives way to multi-modal fluctuations in space and time.

These kinetic simulation results show that the ion dynamics and fields in this Z-pinch system evolve in a way that is qualitatively consistent with the physically expected behavior. At the same time, the simulations yield a vast amount of information regarding the details of ion dynamics in an axisymmetric setting. It is worth noting that our ability to analytically predict the kinetic behavior of axisymmetric systems in a quantitative way is rather limited, particularly in instances where the plasma is warm, non-uniform, and nonlinear effects are important [93]. This is why simulation capabilities such as these are critical to the development of a more complete understanding of plasma phenomena.

5. Conclusions

A fourth-order finite-volume Vlasov–Poisson solver is successfully developed for simulating axisymmetric plasma configurations in (r, v_r, v_θ) cylindrical phase space coordinates. To ensure discrete conservation of the distribution function, the Vlasov equation is first cast into conservation-law form, which is derived through a phase space coordinate transformation. The spatial discretization relies on fifth-order polynomial reconstructions of the solution and a fourth-order quadrature rule that accounts for variations of the flux along the surface of a cell face. The quadrature rule is based on integrals of Taylor series expansions of functions and products of functions. The method provides a means of implementing high-order specular reflection boundary conditions, which are critical for adequately capturing plasma dynamics at the axis and for being able to simulate a closed system.

The solution is advanced forward in time using a fourth-order explicit Runge–Kutta scheme. The choice of explicit method places stringent constraints on the time step size because of the large advection speeds near the axis resulting from centrifugal and Coriolis accelerations. Thereby increasing resolution requires decreasing the time step size. These constraints on time step are alleviated in part through the use of high-order methods, which allow for enhanced accuracy simulations at modest resolutions and can be further alleviated through the use of implicit time-advance methods, which are not explored here.

The fourth-order discretization is applied to a uniform neutral gas system to quantitatively assess the algorithm's ability to preserve an equilibrium distribution function. It is noted that in cylindrical phase space coordinates, even a spatially-uniform Maxwellian distribution function will exhibit advection due to the presence of centrifugal and Coriolis forces. Analytically, equilibrium is satisfied by the cancellation of multiple terms in the Vlasov equation – a cancellation that is not guaranteed in the context of a numerical discretization as numerical error alone can cause an equilibrium distribution function to evolve. Notably in a collisionless system there are no mechanisms to drive a function toward a given equilibrium state. As a result, equilibrium is not maintained by the finite-volume method, but the simulation results are shown to converge to equilibrium at a rate that is consistent with a fourth-order accurate discretization.

The algorithm is applied to simulate electrostatic ion confinement in a Z-pinch configuration, a problem in which ions are dynamic and electrons are assumed to be stationary. The distribution function and electric field are demonstrated to converge at fourth-order. The simulation results are consistent with expected behavior in that a peripheral electric field develops, confining ions to the electrons. As it evolves, the ion distribution function exhibits complex structures including local non-Maxwellian features due to phase mixing. Also observed are multi-modal features in the density and electric field and the development of temperature anisotropy due to compression of the collisionless ions. These simulations demonstrate the rich kinetic physics that in many respects can only be accessed through simulations. Because linear theory does not provide a straightforward means to analytically treat warm non-uniform axisymmetric kinetic plasmas, the algorithm described here presents an important and quantitatively verified means of advancing our understanding of unexplained plasma phenomena. Through the development of a robust high-accuracy continuum kinetic algorithm, this work presents an important step toward high-fidelity modeling of more generalized axisymmetric plasma configurations.

References

[1] C. Birdsall, A. Langdon, Plasma Physics via Computer Simulation, McGraw-Hill, New York, NY, 1985.
[2] J.P. Verboncoeur, Particle simulation of plasmas: review and advances, Plasma Phys. Control. Fusion 47 (5A) (2005) A231, http://stacks.iop.org/0741-3335/47/i=5A/a=017.
[3] D. Tskhakaya, K. Matyash, R. Schneider, F. Taccogna, The particle-in-cell method, Contrib. Plasma Phys. 47 (8–9) (2007) 563–594, https://doi.org/10.1002/ctpp.200710072.
[4] A.B. Langdon, Evolution of particle-in-cell plasma simulation, IEEE Trans. Plasma Sci. 42 (5) (2014) 1317–1320, https://doi.org/10.1109/TPS.2014.2314615.
[5] A.J. Klimas, W.M. Farrell, A splitting algorithm for Vlasov simulation with filamentation filtration, J. Comput. Phys. 110 (1) (1994) 150–163, https://doi.org/10.1006/jcph.1994.1011, http://www.sciencedirect.com/science/article/pii/S0021999184710114.
[6] J.W. Schumer, J.P. Holloway, Vlasov simulations using velocity-scaled Hermite representations, J. Comput. Phys. 144 (2) (1998) 626–661, https://doi.org/10.1006/jcph.1998.5925, http://www.sciencedirect.com/science/article/pii/S0021999198959253.
[7] G. Delzanno, Multi-dimensional, fully-implicit, spectral method for the Vlasov–Maxwell equations with exact conservation laws in discrete form, J. Comput. Phys. 301 (C) (2015) 338–356, https://doi.org/10.1016/j.jcp.2015.07.028.
[8] C. Cheng, G. Knorr, The integration of the Vlasov equation in configuration space, J. Comput. Phys. 22 (3) (1976) 330–351, https://doi.org/10.1016/0021-9991(76)90053-X, http://www.sciencedirect.com/science/article/pii/002199917690053X.
[9] E. Sonnendrücker, J. Roche, P. Bertrand, A. Ghizzo, The semi-Lagrangian method for the numerical resolution of the Vlasov equation, J. Comput. Phys. 149 (2) (1999) 201–220, https://doi.org/10.1006/jcph.1998.6148, http://www.sciencedirect.com/science/article/pii/S0021999198961484.
[10] F. Filbet, E. Sonnendrücker, P. Bertrand, Conservative numerical schemes for the Vlasov equation, J. Comput. Phys. 172 (1) (2001) 166–187, https://doi.org/10.1006/jcph.2001.6818, http://www.sciencedirect.com/science/article/pii/S0021999101968184.

[11] F. Filbet, E. Sonnendrücker, Comparison of Eulerian Vlasov solvers, Comput. Phys. Commun. 150 (3) (2003) 247–266, https://doi.org/10.1016/S0010-4655(02)00694-X, http://www.sciencedirect.com/science/article/pii/S001046550200694X.

[12] J. Banks, J. Hittinger, A new class of nonlinear finite-volume methods for Vlasov simulation, IEEE Trans. Plasma Sci. 38 (9) (2010) 2198–2207, https://doi.org/10.1109/TPS.2010.2056937.

[13] G.V. Vogman, P. Colella, U. Shumlak, Dory–Guest–Harris instability as a benchmark for continuum kinetic Vlasov–Poisson simulations of magnetized plasmas, J. Comput. Phys. 277 (2014) 101–120, https://doi.org/10.1016/j.jcp.2014.08.014, http://www.sciencedirect.com/science/article/pii/S0021999114005609.

[14] R.E. Heath, I.M. Gamba, P.J. Morrison, C. Michler, A discontinuous Galerkin method for the Vlasov–Poisson system, J. Comput. Phys. 231 (4) (2012) 1140–1174.

[15] Y. Cheng, I. Gamba, F. Li, P. Morrison, Discontinuous Galerkin methods for the Vlasov–Maxwell equations, SIAM J. Numer. Anal. 52 (2) (2014) 1017–1049, https://doi.org/10.1137/130915091.

[16] J. Juno, A. Hakim, J. TenBarge, E. Shi, W. Dorland, Discontinuous Galerkin algorithms for fully kinetic plasmas, J. Comput. Phys. 353 (Supplement C) (2018) 110–147, https://doi.org/10.1016/j.jcp.2017.10.009, http://www.sciencedirect.com/science/article/pii/S0021999117307477.

[17] Y. Cheng, A.J. Christlieb, X. Zhong, Energy-conserving discontinuous Galerkin methods for the Vlasov–Ampère system, J. Comput. Phys. 256 (2014) 630–655, https://doi.org/10.1016/j.jcp.2013.09.013, http://www.sciencedirect.com/science/article/pii/S0021999113006189.

[18] J.A.F. Hittinger, J.W. Banks, Block-structured adaptive mesh refinement algorithms for Vlasov simulation, J. Comput. Phys. 241 (2013) 118–140, https://doi.org/10.1016/j.jcp.2013.01.030, http://www.sciencedirect.com/science/article/pii/S0021999113000740.

[19] M.R. Dorr, R.H. Cohen, P. Colella, M.A. Dorf, J.A.F. Hittinger, D.F. Martin, Numerical simulation of phase space advection in gyrokinetic models of fusion plasmas, in: Proceedings of the 2010 Scientific Discovery Through Advanced Computing (SciDAC) Conference, Chattanooga, TN, 2010, pp. 11–15.

[20] M.A. Dorf, M.R. Dorr, J.A. Hittinger, R.H. Cohen, T.D. Rognlien, Continuum kinetic modeling of the tokamak plasma edge, Phys. Plasmas 23 (5) (2016) 056102, https://doi.org/10.1063/1.4943106.

[21] M.R. Dorr, P. Colella, M.A. Dorf, D. Ghosh, J.A. Hittinger, P.O. Schwartz, High-order discretization of a gyrokinetic Vlasov model in edge plasma geometry, arXiv preprint arXiv:1712.01978.

[22] A.G. Peeters, Y. Camenen, F.J. Casson, W.A. Hornsby, A.P. Snodin, D. Strintzi, G. Szepesi, The nonlinear gyro-kinetic flux tube code GKW, Comput. Phys. Commun. 180 (12) (2009) 2650–2672, https://doi.org/10.1016/j.cpc.2009.07.001, 40 Years of CPC: a celebratory issue focused on quality software for high performance, grid and novel computing architectures, http://www.sciencedirect.com/science/article/pii/S0010465509002112.

[23] T. Görler, X. Lapillonne, S. Brunner, T. Dannert, F. Jenko, F. Merz, D. Told, The global version of the gyrokinetic turbulence code GENE, J. Comput. Phys. 230 (18) (2011) 7053–7071, https://doi.org/10.1016/j.jcp.2011.05.034, http://www.sciencedirect.com/science/article/pii/S0021999111003457.

[24] J. Candy, R. Waltz, An Eulerian gyrokinetic-Maxwell solver, J. Comput. Phys. 186 (2) (2003) 545–581, https://doi.org/10.1016/S0021-9991(03)00079-2, http://www.sciencedirect.com/science/article/pii/S0021999103000792.

[25] J.-M. Qiu, A. Christlieb, A conservative high order semi-Lagrangian WENO method for the Vlasov equation, J. Comput. Phys. 229 (4) (2010) 1130–1149, https://doi.org/10.1016/j.jcp.2009.10.016, http://www.sciencedirect.com/science/article/pii/S0021999109005610.

[26] J.A. Rossmanith, D.C. Seal, A positivity-preserving high-order semi-Lagrangian discontinuous Galerkin scheme for the Vlasov–Poisson equations, J. Comput. Phys. 230 (16) (2011) 6203–6232, https://doi.org/10.1016/j.jcp.2011.04.018, http://www.sciencedirect.com/science/article/pii/S0021999111002579.

[27] J.P. Verboncoeur, Symmetric spline weighting for charge and current density in particle simulation, J. Comput. Phys. 174 (1) (2001) 421–427, https://doi.org/10.1006/jcph.2001.6923, http://www.sciencedirect.com/science/article/pii/S0021999101969232.

[28] G. Jacobs, J. Hesthaven, High-order nodal discontinuous Galerkin particle-in-cell method on unstructured grids, J. Comput. Phys. 214 (1) (2006) 96–121, https://doi.org/10.1016/j.jcp.2005.09.008, http://www.sciencedirect.com/science/article/pii/S0021999105004250.

[29] C. Cornet, D.T.K. Kwok, A new algorithm for charge deposition for multiple-grid method for PIC simulations in r–z cylindrical coordinates, J. Comput. Phys. 225 (1) (2007) 808–828, https://doi.org/10.1016/j.jcp.2007.01.004, http://www.sciencedirect.com/science/article/pii/S0021999107000058.

[30] S.J. Araki, R.E. Wirz, Cell-centered particle weighting algorithm for PIC simulations in a non-uniform 2D axisymmetric mesh, J. Comput. Phys. 272 (Supplement C) (2014) 218–226, https://doi.org/10.1016/j.jcp.2014.04.037, http://www.sciencedirect.com/science/article/pii/S0021999114003003.

[31] C.A. Fichtl, J.M. Finn, K.L. Cartwright, An arbitrary curvilinear-coordinate method for particle-in-cell modeling, Comput. Sci. Discov. 5 (1) (2012) 014011, http://stacks.iop.org/1749-4699/5/i=1/a=014011.

[32] C.S. Meierbachtol, D. Svyatskiy, G.-L. Delzanno, L.J. Vernon, J.D. Moulton, An electrostatic particle-in-cell code on multi-block structured meshes, J. Comput. Phys. 350 (Supplement C) (2017) 796–823, https://doi.org/10.1016/j.jcp.2017.09.016, http://www.sciencedirect.com/science/article/pii/S0021999117306757.

[33] L. Chacon, G. Chen, D. Barnes, A charge- and energy-conserving implicit, electrostatic particle-in-cell algorithm on mapped computational meshes, J. Comput. Phys. 233 (Supplement C) (2013) 1–9, https://doi.org/10.1016/j.jcp.2012.07.042, http://www.sciencedirect.com/science/article/pii/S0021999112004275.

[34] J.-L. Vay, D.P. Grote, R.H. Cohen, A. Friedman, Novel methods in the particle-in-cell accelerator code-framework Warp, Comput. Sci. Discov. 5 (1) (2012) 014019, http://stacks.iop.org/1749-4699/5/i=1/a=014019.

[35] A. Davidson, A. Tableman, W. An, F. Tsung, W. Lu, J. Vieira, R. Fonseca, L. Silva, W. Mori, Implementation of a hybrid particle code with a PIC description in r–z and a gridless description in ϕ into OSIRIS, J. Comput. Phys. 281 (Supplement C) (2015) 1063–1077, https://doi.org/10.1016/j.jcp.2014.10.064, http://www.sciencedirect.com/science/article/pii/S0021999114007529.

[36] H.A. Davis, R.R. Bartsch, L.E. Thode, E.G. Sherwood, R.M. Stringfield, High-power microwave generation from a virtual cathode device, Phys. Rev. Lett. 55 (1985) 2293–2296, https://doi.org/10.1103/PhysRevLett.55.2293, https://link.aps.org/doi/10.1103/PhysRevLett.55.2293.

[37] T.A. van der Straaten, N.F. Cramer, I.S. Falconer, B.W. James, The cylindrical DC magnetron discharge: I. particle-in-cell simulation, J. Phys. D, Appl. Phys. 31 (2) (1998) 177, http://stacks.iop.org/0022-3727/31/i=2/a=004.

[38] T.P. Fleming, P.J. Mardahl, L. Bowers, K.L. Cartwright, M.T. Bettencourt, M.D. Haworth, Virtual prototyping of novel cathode designs for the relativistic magnetron, Comput. Sci. Eng. 9 (6) (2007) 18–28, https://doi.org/10.1109/MCSE.2007.131, http://aip.scitation.org/doi/abs/10.1109/MCSE.2007.131.

[39] T.P. Fleming, M.R. Lambrecht, K.L. Cartwright, Numerical simulations of a relativistic inverted magnetron, IEEE Trans. Plasma Sci. 38 (7) (2010) 1563–1573, https://doi.org/10.1109/TPS.2010.2048209.

[40] G. Singh, S. Chaturvedi, Particle-in-cell simulations for virtual cathode oscillator including foil ablation effects, Phys. Plasmas 18 (6) (2011) 063104, https://doi.org/10.1063/1.3595237.

[41] J.C. Adam, A. Héron, G. Laval, Study of stationary plasma thrusters using two-dimensional fully kinetic simulations, Phys. Plasmas 11 (1) (2004) 295–305, https://doi.org/10.1063/1.1632904.

[42] I.D. Kaganovich, Y. Raitses, D. Sydorenko, A. Smolyakov, Kinetic effects in a Hall thruster discharge, Phys. Plasmas 14 (5) (2007) 057104, https://doi.org/10.1063/1.2709865.

[43] P. Coche, L. Garrigues, A two-dimensional (azimuthal-axial) particle-in-cell model of a Hall thruster, Phys. Plasmas 21 (2) (2014) 023503, https://doi.org/10.1063/1.4864625.

[44] D.L. Bruhwiler, R.E. Giacone, J.R. Cary, J.P. Verboncoeur, P. Mardahl, E. Esarey, W.P. Leemans, B.A. Shadwick, Particle-in-cell simulations of plasma accelerators and electron-neutral collisions, Phys. Rev. Spec. Top., Accel. Beams 4 (2001) 101302, https://doi.org/10.1103/PhysRevSTAB.4.101302.

[45] J.-L. Vay, P. Colella, J.W. Kwan, P. McCorquodale, D.B. Serafini, A. Friedman, D.P. Grote, G. Westenskow, J.-C. Adam, A. Héron, I. Haber, Application of adaptive mesh refinement to particle-in-cell simulations of plasmas and beams, Phys. Plasmas 11 (5) (2004) 2928–2934, https://doi.org/10.1063/1.1689669.

[46] J.-L. Vay, R. Lehe, H. Vincenti, B. Godfrey, I. Haber, P. Lee, Recent advances in high-performance modeling of plasma-based acceleration using the full PIC method, in: 2nd European Advanced Accelerator Concepts Workshop – EAAC 2015, Nucl. Instrum. Methods Phys. Res., Sect. A, Accel. Spectrom. Detect. Assoc. Equip. 829 (Supplement C) (2016) 353–357, https://doi.org/10.1016/j.nima.2015.12.033, http://www.sciencedirect.com/science/article/pii/S0168900215016046.

[47] D.-Y. Na, Y.A. Omelchenko, H. Moon, B.-H.V. Borges, F.L. Teixeira, Axisymmetric charge-conservative electromagnetic particle simulation algorithm on unstructured grids: application to microwave vacuum electronic devices, J. Comput. Phys. 346 (Supplement C) (2017) 295–317, https://doi.org/10.1016/j.jcp.2017.06.016, http://www.sciencedirect.com/science/article/pii/S0021999117304618.

[48] T.D. Pointon, W.A. Stygar, R.B. Spielman, H.C. Ives, K.W. Struve, Particle-in-cell simulations of electron flow in the post-hole convolute of the Z accelerator, Phys. Plasmas 8 (10) (2001) 4534–4544, https://doi.org/10.1063/1.1401118.

[49] T.D. Pointon, W.L. Langston, M.E. Savage, Computer simulations of the magnetically insulated transmission lines and post-hole convolute of ZR, in: 2007 16th IEEE International Pulsed Power Conference, vol. 1, 2007, pp. 165–170.

[50] E.A. Madrid, D.V. Rose, D.R. Welch, R.E. Clark, C.B. Mostrom, W.A. Stygar, M.E. Cuneo, M.R. Gomez, T.P. Hughes, T.D. Pointon, D.B. Seidel, Steady-state modeling of current loss in a post-hole convolute driven by high power magnetically insulated transmission lines, Phys. Rev. Spec. Top., Accel. Beams 16 (2013) 120401, https://doi.org/10.1103/PhysRevSTAB.16.120401.

[51] D.V. Rose, E.A. Madrid, D.R. Welch, R.E. Clark, C.B. Mostrom, W.A. Stygar, M.E. Cuneo, Computational analysis of current-loss mechanisms in a post-hole convolute driven by magnetically insulated transmission lines, Phys. Rev. Spec. Top., Accel. Beams 18 (2015) 030402, https://doi.org/10.1103/PhysRevSTAB.18.030402.

[52] D. Nielsen, J. Green, O. Buneman, Dynamic evolution of a Z pinch, Phys. Rev. Lett. 42 (1979) 1274–1277, https://doi.org/10.1103/PhysRevLett.42.1274.

[53] T.D. Arber, Hybrid simulation of the nonlinear evolution of a collisionless, large Larmor radius Z pinch, Phys. Rev. Lett. 77 (1996) 1766–1768, https://doi.org/10.1103/PhysRevLett.77.1766.

[54] Y. Mizuguchi, J.-I. Sakai, H.R. Yousefi, T. Haruki, K. Masugata, Simulation of high-energy proton production by fast magnetosonic shock waves in pinched plasma discharges, Phys. Plasmas 14 (3) (2007) 032704, https://doi.org/10.1063/1.2716673.

[55] D. Welch, D. Rose, R. Clark, C. Mostrom, W. Stygar, R. Leeper, Fully kinetic particle-in-cell simulations of a deuterium gas puff Z pinch, Phys. Rev. Lett. 103 (25) (2009) 255002, https://doi.org/10.1103/PhysRevLett.103.255002.

[56] A. Schmidt, V. Tang, D. Welch, Fully kinetic simulations of dense plasma focus Z-pinch devices, Phys. Rev. Lett. 109 (2012) 205003, https://doi.org/10.1103/PhysRevLett.109.205003.

[57] H. Ohtani, R. Horiuchi, T. Sato, Self-generation of hollow current profile and tilt instability in field-reversed configuration, Phys. Plasmas 10 (1) (2003) 145–156, https://doi.org/10.1063/1.1526703.

[58] L.C. Steinhauer, Review of field-reversed configurations, Phys. Plasmas 18 (7) (2011) 070501, https://doi.org/10.1063/1.3613680.

[59] F. Filbet, J.-L. Lemaire, E. Sonnendrücker, Direct axisymmetric Vlasov simulations of space charge dominated beams, Springer, Berlin/Heidelberg, 2002, pp. 305–314.

[60] L. Mieussens, Discrete-velocity models and numerical schemes for the Boltzmann-BGK equation in plane and axisymmetric geometries, J. Comput. Phys. 162 (2) (2000) 429–466, https://doi.org/10.1006/jcph.2000.6548, http://www.sciencedirect.com/science/article/pii/S0021999100965483.

[61] M. Shoucri, H. Gerhauser, K.-H. Finken, Study of the generation of a charge separation and electric field at a plasma edge using Eulerian Vlasov codes in cylindrical geometry, in: Proceedings of the 18th International Conference on the Numerical Simulation of Plasmas, Comput. Phys. Commun. 164 (1) (2004) 138–149, https://doi.org/10.1016/j.cpc.2004.06.022, http://www.sciencedirect.com/science/article/pii/S0010465504002723.

[62] F. Valentini, P. Veltri, A. Mangeney, A numerical scheme for the integration of the Vlasov–Poisson system of equations, in the magnetized case, J. Comput. Phys. 210 (2) (2005) 730–751, https://doi.org/10.1016/j.jcp.2005.05.014, http://www.sciencedirect.com/science/article/pii/S0021999105002597.

[63] I. Larina, V. Rykov, A numerical method for calculating axisymmetric rarefied gas flows, Ž. Vyčisl. Mat. Mat. Fiz. 38 (8) (1998) 1391–1403.

[64] I. Larina, V. Rykov, Numerical solution method of axially simmetric problems for the Boltzmann equation, Mat. Model. 16 (6) (2004) 65–68.

[65] P. Colella, M. Dorr, J. Hittinger, D. Martin, High-order, finite-volume methods in mapped coordinates, J. Comput. Phys. 230 (8) (2011) 2952–2976, https://doi.org/10.1016/j.jcp.2010.12.044, http://www.sciencedirect.com/science/article/pii/S0021999111000064.

[66] M. Vinokur, Conservation equations of gasdynamics in curvilinear coordinate systems, J. Comput. Phys. 14 (2) (1974) 105–125, https://doi.org/10.1016/0021-9991(74)90008-4, http://www.sciencedirect.com/science/article/pii/0021999174900084.

[67] A.A. Vlasov, Statistical Distribution Functions, Nauka, Moscow, 1966.

[68] M.N. Kogan, Rarefied Gas Dynamics: Dinamika Razrezennogo Gaza, Plenum Press, 1969, Transl. from Russian.

[69] Y. Sone, Kinetic Theory and Fluid Dynamics, Springer Science & Business Media, 2012.

[70] E.M. Shakhov, Boltzmann equation and moment equations in curvilinear coordinates, Fluid Dyn. 2 (2) (1967) 107–109, https://doi.org/10.1007/BF01015156.

[71] G.V. Vogman, Fourth-order conservative Vlasov–Maxwell solver for Cartesian and cylindrical phase space coordinates, Ph.D. thesis, University of California Berkeley, 2016.

[72] J. Cooper, A. Klimas, Boundary value problems for the Vlasov–Maxwell equation in one dimension, J. Math. Anal. Appl. 75 (2) (1980) 306–329, https://doi.org/10.1016/0022-247X(80)90082-7, http://www.sciencedirect.com/science/article/pii/0022247X80900827.

[73] Y. Guo, Global weak solutions of the Vlasov–Maxwell system with boundary conditions, Commun. Math. Phys. 154 (2) (1993) 245–263, https://doi.org/10.1007/BF02096997.

[74] T.T. Nguyen, W.A. Strauss, Stability analysis of collisionless plasmas with specularly reflecting boundary, SIAM J. Math. Anal. 45 (2) (2013) 777–808.

[75] C. Cercignani, The Boltzmann equation, in: The Boltzmann Equation and Its Applications, Springer, 1988, pp. 40–103.

[76] P. McCorquodale, P. Colella, A high-order finite-volume method for conservation laws on locally refined grids, Commun. Appl. Math. Comput. Sci. 6 (1) (2011) 1–25.

[77] M. Dorr, P. Colella, J. Hittinger, D. Martin, P. McCorquodale, High-resolution methods for phase space problems in complex geometries, Tech. rep., Lawrence Livermore National Laboratory (LLNL), Livermore, CA, 2012.

[78] J. Casper, H. Atkins, A finite-volume high-order ENO scheme for two-dimensional hyperbolic systems, J. Comput. Phys. 106 (1) (1993) 62–76, https://doi.org/10.1006/jcph.1993.1091, http://www.sciencedirect.com/science/article/pii/S0021999183710910.

[79] L. Ivan, C.P. Groth, High-order solution-adaptive central essentially non-oscillatory (CENO) method for viscous flows, J. Comput. Phys. 257 (2014) 830–862, https://doi.org/10.1016/j.jcp.2013.09.045, http://www.sciencedirect.com/science/article/pii/S0021999113006591.

[80] C.-W. Shu, Essentially non-oscillatory and weighted essentially non-oscillatory schemes for hyperbolic conservation laws, in: A. Quarteroni (Ed.), Advanced Numerical Approximation of Nonlinear Hyperbolic Equations, in: Lecture Notes in Mathematics, vol. 1697, Springer, Berlin/Heidelberg, 1998, pp. 325–432.

[81] C.-W. Shu, High-order finite difference and finite volume WENO schemes and discontinuous Galerkin methods for CFD, Int. J. Comput. Fluid Dyn. 17 (2) (2003) 107–118, https://doi.org/10.1080/1061856031000104851.

[82] E.F. Toro, R.C. Millington, L.A.M. Nejad, Towards Very High Order Godunov Schemes, Springer US, Boston, MA, 2001, pp. 907–940.

[83] V.A. Titarev, E.F. Toro, ADER schemes for three-dimensional non-linear hyperbolic systems, J. Comput. Phys. 204 (2) (2005) 715–736, https://doi.org/10.1016/j.jcp.2004.10.028, http://www.sciencedirect.com/science/article/pii/S0021999104004358.

[84] C. Chaplin, P. Colella, A single-stage flux-corrected transport algorithm for high-order finite-volume methods, Commun. Appl. Math. Comput. Sci. 12 (1) (2017) 1–24.

[85] M. Oevermann, R. Klein, A Cartesian grid finite volume method for elliptic equations with variable coefficients and embedded interfaces, J. Comput. Phys. 219 (2) (2006) 749–769, https://doi.org/10.1016/j.jcp.2006.04.010, http://www.sciencedirect.com/science/article/pii/S0021999106002129.

[86] R. Ewing, O. Iliev, R. Lazarov, A modified finite volume approximation of second-order elliptic equations with discontinuous coefficients, SIAM J. Sci. Comput. 23 (4) (2001) 1335–1351, https://doi.org/10.1137/S1064827599353877.

[87] F. Gibou, R.P. Fedkiw, L.-T. Cheng, M. Kang, A second-order-accurate symmetric discretization of the Poisson equation on irregular domains, J. Comput. Phys. 176 (1) (2002) 205–227, https://doi.org/10.1006/jcph.2001.6977, http://www.sciencedirect.com/science/article/pii/S0021999101969773.

[88] J.M. Blondin, E.A. Lufkin, The piecewise-parabolic method in curvilinear coordinates, Astrophys. J. Suppl. Ser. 88 (1993) 589–594, https://doi.org/10.1086/191834.

[89] A. Mignone, High-order conservative reconstruction schemes for finite volume methods in cylindrical and spherical coordinates, J. Comput. Phys. 270 (2014) 784–814, https://doi.org/10.1016/j.jcp.2014.04.001, http://www.sciencedirect.com/science/article/pii/S0021999114002538.

[90] M.G. Haines, A review of the dense Z-pinch, Plasma Phys. Control. Fusion 53 (9) (2011) 093001, http://stacks.iop.org/0741-3335/53/i=9/a=093001.

[91] D.D. Ryutov, Characterizing the plasmas of dense Z-pinches, IEEE Trans. Plasma Sci. 43 (8) (2015) 2363–2384, https://doi.org/10.1109/TPS.2015.2453265.

[92] R. Goldston, P. Rutherford, Introduction to Plasma Physics, Taylor and Francis Group, 1995.

[93] R.C. Davidson, Physics of Nonneutral Plasmas, Imperial College Press, London, 2001.